Studies of Nanosecond Pulsed Plasmas at Atmospheric-Pressure Using Laser Thomson Scattering

ボロウキ, ニマ

Studies of Nanosecond Pulsed Plasmas at Atmospheric-Pressure Using Laser Thomson Scattering

Nima Bolouki

Department of Applied Science for Electronics and Materials

Interdisciplinary Graduate School of Engineering Sciences

Kyushu University

Under the Supervision of

Professor Kiichiro Uchino

March 2015

Contents

Acknowledgments

Abstract

Non-thermal atmospheric-pressure plasmas have received much attentions due to their substantial capacity for application in the fields of plasmas, such as plasma nanoscience, plasma medicine, and plasma chemistry. In applications of such plasma sources, radicals generated inside the plasma play key roles in the resultant of chemical reactions. Since the generation of radicals is governed by the presence of free electrons in plasmas, measurements of the electron density (n_e) and electron temperature (T_e) are essential for understanding plasma behavior. On the other hand, the most input power is supplied by electrons in non-thermal plasmas. Hence, to improve plasma devices efficiency, knowing the plasma parameters are so important.

The purpose of this research is applying laser Thomson scattering (LTS) method as a diagnostics system to measure n_e and T_e in non-thermal atmospheric pressure plasmas such as capacity coupled discharge (CCD), dielectric barrier discharge (DBD), and the early stage of the high-voltage waveform that is called primary streamer.

Capacity coupled discharge (CCD) has been selected as a non-thermal atmospheric pressure plasma. Since CCD does not have a dielectric layer between discharge electrodes, the formation time and the spatial position of the CCD plasma could be controlled. The spatial distribution and temporal variation of n_e and T_e have been examined. At the center of the discharge, n_e and T_e has been estimated to be 4.6 ($\pm$ 0.6) $\times$ 10^{22} m^{-3} and 1.7 ($\pm$ 0.3) eV, respectively, at the time of 15 ns after the start of the discharge. A significant deference has been observed in temporal behavior between n_e and T_e after the discharge generation. Temporal behavior of n_e and T_e are discussed on the basis of two recombination processes: three-body electron-ion recombination because of high electron density and electron-ion dissociative recombination due to the formation of dimer ion in high pressure. Both of these mechanisms are operative in this system. The rapid decrease of T_e until 35 ns can be explained by two processes: the termination of power input to the discharge and the energy transfer by elastic collisions between the electrons and neutral particles or ions. Assuming the above values (n_e and T_e), the total collision frequency is estimated to be approximately 1×10^{12} Hz. The thermal relaxation time of electrons with neutral particles is calculated to be less than 20 ns. Considering this time, it is understood that the energy of the

electrons can be transferred to the neutral particles in a short time. On the other hand, the decrease of T_e is gradual after 35 ns. It has been suggested that the three-body recombination process can be a heating source for electrons because the third electron of the process can obtain a part of the ionization-energy released by the process. The obtained results are useful for discussing the particle and power balances of the discharge plasma.

In addition, LTS measurements have been successfully applied to DBD. Temporal evolution of electron density and temperature were found to be similar to those of CCD. Because the total current charge for DBD was a fifth of that of CCD described above, the electron density of DBD was relatively low and was $(1.03 \pm 0.08) \times 10^{22}$ m^{-3} at the center of the discharge.

Furthermore, the LTS method have been developed to diagnose streamer plasmas. The LTS signals were detected clearly and the values of n_e and T_e of the streamer were obtained for the first time. In order to avoid laser perturbation and obtain sufficient intensity of Thomson scattering signal, two cylindrical lenses have been employed to optimize spot size of a probing laser at a focusing point. The electron density and electron temperature were successfully measured to be $\sim 10^{18}$ m^{-3} and ~ 2 eV, respectively in the initial stage of the primary streamer. As time passes, the electron density and electron temperature decreased to the minimum. These features of the streamer were found to be consistent with reported simulation-results.

Chapter 1

Introduction

Over 15 billion years ago the matter which composed the universe was so hot that everything was in the form of plasma. Nowadays, more than 99% of the universe is composed of plasma. In a simple definition, when we heat up a solid, it turns into a liquid. Further heating turns the liquid into a gas and more heating leads to a plasma. A plasma medium contains very large number of free electrons, positively charged ions and neutral atoms or molecules which governed by electromagnetic force. In this phase of matter, the heat is the expression of the separate electron and ion motions. Plasma is essential to explain the universe and also is extensively used in industry to improve the standard and quality of life.

1.1 Electrical discharge characterizations

An effective method to create plasmas is through electrical breakdown of gases, which is the process of producing charged particles by applying a strong electric field to the gases. Electrical discharges have been investigated extensively since the 19th century, when vacuum pumps and electricity sources became available. In the early 1900s, Townsend described the breakdown mechanism. In order to understand breakdown phenomena in gases, the electrical properties of gases should be studied. The processes by which high currents are produced in gases are essential. The electrical discharges in gases are two types: 1. Non-sustaining discharges 2. Self-sustaining discharges. The breakdown in a gas is the transition of a non-sustaining discharge into a self-sustaining discharge. The formation of high current in a breakdown is due to the ionization in which electrons and ions are created from neutral atoms or molecules, and their migration to the anode and cathode respectively leads to high current. Townsend theory and streamer theory are the present two types of theories which explain the mechanism of breakdown under different conditions as pressure, temperature, electrode configurations, electrode surface properties and availability of initial conducting particles. The operating pressure could be low, around

atmospheric or high. The distinction between atmospheric and low pressure can be made when considering the pressure at which the plasma is generated. In plasmas, the electrons receive high energies. If the electrons and the other species such as molecules and ions obtain a thermal energy distribution at the same high temperature, the plasma is called thermal, indicating that the plasma is in thermal equilibrium. If only the electrons have high energy and the other species temperature remain in room temperature (about 300 K), the plasma is called non-thermal or non-equilibrium plasma. Dielectric Barrier Discharge (DBD) is typical plasma in non-thermal category. Fig.1.1 shows voltage-time characteristics of plasma in atmospheric pressure. It gives an overview of atmospheric pressure plasmas. Traditional plasma sources include plasma torches, corona discharges, and dielectric barrier discharges. Three good review papers about atmospheric pressure plasmas and plasma sources can be found in Ref. [1- 3].
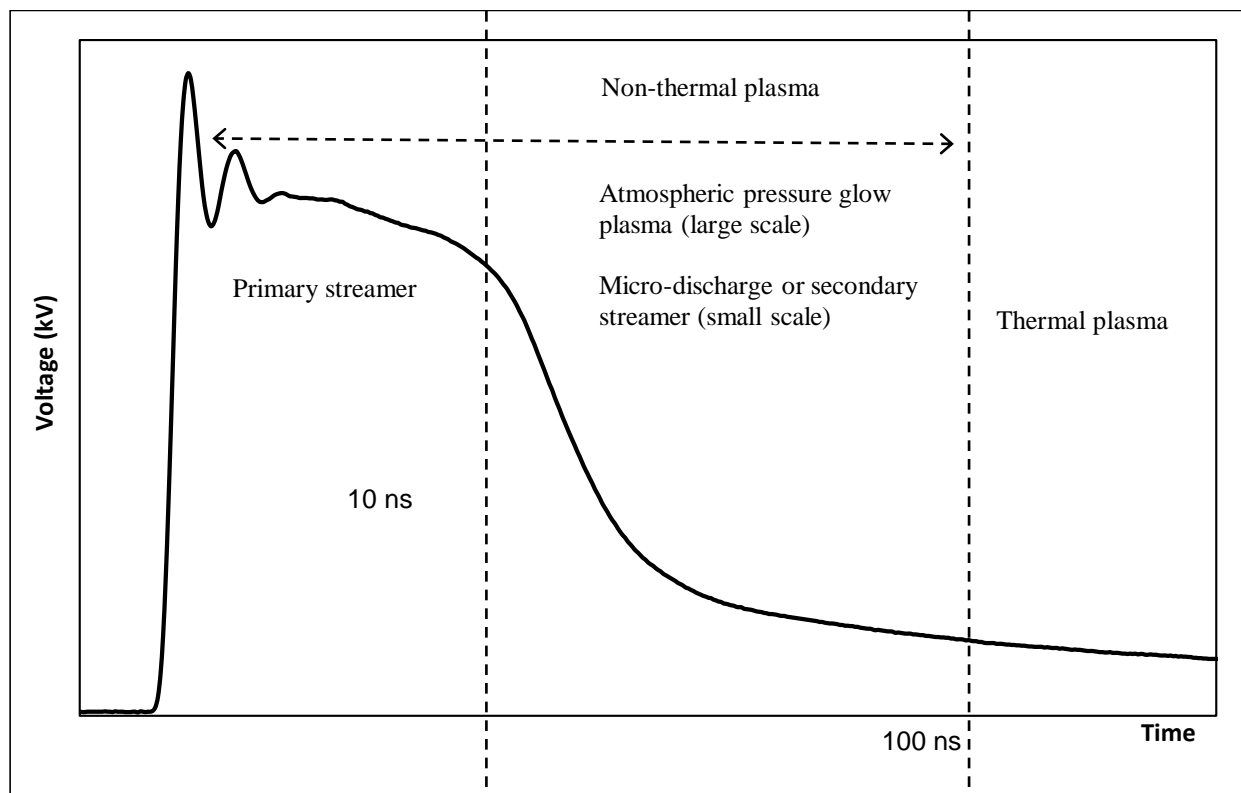
Fig.1.1 Voltage-time characteristics in atmospheric pressure plasmas

1.2 Streamer

The initial stage of the electrical breakdown is the development of ionization waves, also known as streamer discharges. In order to understand the streamer structure, it is necessary to distinguish different stages of streamer. Based on the steamer dynamics, there are three stages for streamer phase: 1) the electron avalanche phase 2) the streamer propagation that is called primary streamer 3) the streamers have crossed the gap. This final stage of evolution is also known as a secondary streamer or micro discharge.

Townsend theory for breakdown and development of ionization process cannot explain streamer phenomena. So the streamer theory was proposed to explain these observed phenomena. The theory predicts the development of a filamentary discharge directly from a single avalanche in which the space charges develop by the avalanche itself is said to transform the avalanche into a plasma streamer. Approximately, $10^3 - 10^6$ free electrons/m^3 are always present in environment due to cosmic ray and UV radiation. A free electron will accelerate in an electric field. Hence, it gains energy and collide with a molecule. It can release an electron provided that it has received sufficient energy during acceleration. As a result of the ionization, two free electrons are created in the electric field. Both electrons accelerate in the electric field. During the passing through the electric field, the electron may undergo multiple ionization collisions. Generally, the electrons in the avalanche due to high mobility move very fast compared with the positive ions. By passing the time when the electrons reach the anode, the positive ions are still in the original positions and form a positive space charge at the anode. This enhances the field, and the secondary avalanches are formed from a few electrons produced due to photo-ionization in the space charge region. This happens first near the anode where the space charges are in maximum and a further increase in the space charges. This process is so fast and the positive space charges extend to the cathode rapidly resulting in the formation of a streamer. As a result, narrow luminous tracks occurring at breakdown are called streamers. As soon as the streamer head approaches to the cathode, a cathode spot is formed and a streamer of electrons rushes from cathode to neutralize the positive space charges in the streamer. It leads to a filamentary discharge and breakdown occurs.

Generally, it is assumed that for *pd* values below 10 Torr-m and gas pressures varying from 0.01 to 300 Torr, the Townsend mechanism operates, while at higher pressures and *pd* values the

streamer mechanism plays the dominant role in explaining the breakdown phenomena. However, some unclear issues still exist in these statements.

For example, in air at atmospheric pressure transition to streamer occur when more then 10^{8} electrons accumulated in avalanche. The streamer velocity is in the range 10^{5}-10^{6} m/s, the radius of the propagating streamer head and the resulting ionized channel is about 10^{-4}-10^{-3} m. The reduced field E/N at the streamer head can reach 500 to 800 Td (1 Townsend or Td corresponds to 10^{-21} V.m^{2}), a value that is several times higher than the reduced field at breakdown (about 100 to 200 Td). Table 1 shows some properties of streamer in air at atmospheric pressure.

Table 1: Streamer properties in air at atmospheric pressure

Duration: 10-20 ns	Total Charge: 10^{-10}-10^{-9} C
Filament radius: 0.1 mm	Electron density: 10^{20}-10^{21} m^{-3}
Peak current: 0.1 A	Mean Electron energy: 1-10 eV
Current density: 10^{6}-10^{7} A/m^{2}	Streamer velocity: 10^{5}-10^{6} m/s

To continue streamers propagating, being available of new free electrons which can develop into an avalanche is important. Hence, it is necessary to distinguish between cathode directed streamers CDS (positive streamers) and anode directed streamers ADS (negative streamers). The difference is due to the applied voltage polarity on the electrode (active electrode). There is a main difference between CDS and ADS when we look at the streamer propagation direction relative to the applied electric field. For the CDS these directions are parallel, but for the ADS are antiparallel. In addition, at the ADS the electrons travel in the same direction relative to the streamer propagation. The required secondary electrons are generated in the streamer head and

then accelerate in the direction of streamer of propagation. At the CDS, the situation is complicated. The electrons travel in the direction opposite to the streamer. To continue streamer propagating, a mechanism is required that generates free electron in the sheath surrounding the steamer head, which then accelerate and create an avalanche. If the electrons are generated too far from the streamer head, the electric field is too low to obtain a positive net ionization. The suitable region for new avalanche creation is called active region.

1.3 Dielectric barrier discharges (DBD)

The discharge between two electrodes, from which at least one is covered with a dielectric layer, at atmospheric pressure (called dielectric barrier discharge or silent discharge) has been known more than a hundred years. Initial experimental investigations were reported by Siemens in 1857. In that time, they concentrated on the generation of ozone. In recent years, properties of DBD plasmas and its dynamics in different electrode configurations have been investigated numerically by researchers [4-7]. DBD plasma is typically obtained between two parallel electrodes separated by a gap of some millimeters and exited by alternating current (AC) voltage. They are very attractive for industrial applications due to providing non-thermal and non-equilibrium plasma conditions at around atmospheric pressure. The dielectric barrier can be made from glass, quartz, ceramics, or polymer materials of low dielectric loss and high break down strength. The presence of the dielectric leads to the formation of a large number of micro-discharges [8].

1.3.1 Micro-discharge Formation

Many investigations show that at atmospheric pressure electrical breakdown in planar electrode configuration occurs in a large number of nanosecond filaments referred to as a micro-discharge. These micro-discharges are randomly distributed with respect to space and time. Most of the industrial applications of barrier discharges operate in this filamentary mode. The micro-discharges have complex dynamic structure and are formed by channel streamers that repeatedly strike at the same place as the polarity of the applied voltage changes. Thus, it appears to the eye as bright filaments. The extinction voltage of the micro discharges is not far below the voltage of their ignition. Charge accumulation on the surface of the dielectric barrier reduces the electric field at the location of a micro discharge, which results in current termination within tens of

5

nanoseconds after breakdown. The short duration of current in Micro-discharges leads to low heat dissipation, and the DBD plasma remains strongly non-thermal. The nature of the discharge depends on the gas mixture employed, the dielectric, and the operating conditions. Also the number of generated micro-discharges per unit of electrode area and time depends on the power density. The energy density and transferred charges is determined by the gap distance, operating pressure, and dielectric layer properties.

Barrier discharges can exhibit two major discharge modes: streamer (with bright micro-discharges) and glow. The glow mode of DBD is not necessarily uniform, and it can be filamentary. These glow filaments are formed by avalanches rather than streamers. In fact, micro-discharges are initiated by Townsend, not a streamer breakdown. The glow mode by DBDs is usually referred to as the Atmospheric Pressure Glow (APG) [9]. The filamentary mode is a topic for investigations in recent years. Much experimental works have been done in this area [10-15]. Both glow and filamentary discharge modes are formed at atmospheric pressure.

1.4 Atmospheric pressure thermal plasma

Thermal plasmas are partially or strongly ionized gases, usually created by electric arcs at atmospheric or low pressure. If the current in the gap is increased to about 1 A or more, the voltage across the gap reduces suddenly and remains rather weak. In such a condition, the discharge becomes very luminous and noisy. Firstly, the energy given to the plasma is captured by the electrons because of their high mobility (the same as non-thermal plasma). Then, due to the high electron number density, elastic collision frequencies are very high. Therefore, energy transfer leads to an equal distribution of energy and there is thermal equilibrium among all the kinds of particles allowing a single temperature to be defined for the plasma at a given position. A good review paper about thermal plasma can be found in reference [16].

1.5 Applications of atmospheric pressure plasmas

Nowadays, Applications of plasma technologies are numerous and involve many industries. The atmospheric plasma sources based on structure, power supply, plasma temperature, and operating conditions are very different. Therefore, they have wide applications. Although plasmas generated at low pressure show interesting properties, industrial applications working at atmospheric pressure has great advantages. Because the processing can be continuous and

vacuum vessels, pumps are unnecessary. The review and discussion of applications for atmospheric pressure plasmas especially in non-thermal plasma can be found in references [2, 8].

1.5.1 Non-thermal atmospheric pressure plasmas applications

One of the old applications in atmospheric pressure plasma is ozone generator. The discovery of chemical compound of ozone belongs to 1839 and it has been done by Christian Friedrich Schonbein. After that, Werner Siemens, in 1857, proposed a method to generate ozone by passing air or oxygen through an alternative discharge in a DBD plasma. Nowadays, this method still is used in industrial ozone generation.

The dielectric barrier discharges also used for the control of gaseous pollutants and destruction compounds. The early investigations on the destruction of chemical compounds were carried out by Berthelot in 1876. Non-thermal plasmas use most of the discharge energy to produce energetic electrons. The electrons generate reactive free radicals which can decompose toxic compounds.

One of the new applications in DBD plasmas are Plasma displays which utilize Xe VUV radiation to excite phosphor layers deposited inside the tiny gas discharge cells used for individual pixels. In ac plasma displays all electrodes are covered by dielectric layers and sputter resistant MgO coatings. The original idea to use dielectric barrier discharges for large area displays originated at University of Illinois in 1964.

One of the most recent additions to dielectric barrier discharge applications is plasma biomedicine. Recent years, many researches have been done research in cancer cell treatment and wound healing such as bacteria sterilization, blood coagulation, etc under plasma treatment.

A good relevant example of plasma application in high technology is plasma etching in single crystal silicon, which is so important in the fabrication of integrated circuit. Finally, we probably would not have personal computers and cell phones like we have now without plasma processing.

1.6 Diagnostics of non-thermal atmospheric pressure plasmas

There are numerous techniques for plasma characterization that have limited applications in different plasma sources. The diagnostics of atmospheric pressure plasmas requires special and

precise designed experimental techniques and instrumentation. Because, the plasma conditions achieved vary over a wide range. For example, their time scale and the spatial dimensions are such that temporal and spatial resolution of several nanoseconds and microns. Since Langmuir probes (traditional diagnostics in plasma) perturb the plasma enough to generate unreliable results and also indicates that they are problematic for measuring low energy electrons, most of the experimental diagnostics studies on the non-thermal atmospheric pressure plasma are limited to optical and spectroscopic methods to acquire data about densities of different species [17,18]. Although these methods are rather difficult, they provide good information about atomic and molecular species, their excited and ionization states, and some other plasma parameters.

1.6.1 Laser Thomson scattering diagnostics

The most powerful technique for plasma characterization is laser Thomson scattering. It has special place in the laser diagnostics of plasmas. The theory and application of Thomson scattering has long history. The technique is named for J.J. Thomson who introduced the theory for the scattering of electromagnetic radiation by electrons in 1907. The history of this technique belongs to fusion plasma studies. The biggest impact of laser diagnostics for general plasma physicists came when a team of British physicist decisively demonstrated the high performance of T-3 tokamak in the Soviet Union in 1969 by measuring the electron density and temperature of the discharge by Thomson scattering [19].

In diagnostics of high temperature and high electron density thermal plasmas (Arc electrical discharges), a single pulse ruby laser has been employed [20]. In order to use the same technique in glow discharge plasmas, there is a limitation to the number of scattered photons which can be detected. In the steady state in which lower density discharges usually operate, this limitation can be overcome by accumulating data for a large number of laser pulses. This method has enabled Thomson scattering to be applied to various types of glow discharges, such as electron cyclotron resonance (ECR) discharges [21, 22], radio-frequency inductively coupled plasma (ICP) discharges [23-25], a magnetic neutral loop discharge [26], radio-frequency capacity coupled discharges [27], and plasma display panel (PDP) micro-discharge plasmas [28-30] . A Good review and discussion can be found in these references [31-33].

Generally, electrons play a key role in energy transfer and many other processes within plasma sources. Therefore, a complete characterization of any plasma need spatially and temporally resolved data for the electron density and electron temperature as well as electron energy distribution function. Thomson scattering provides a reliable and non-intrusive method that determine inherently radially resolved absolute values for these fundamental parameters, without the assumptions about cylindrical symmetry or thermodynamic conditions in the plasma that are required by the other techniques. These advantages make LTS inherently superior to alternative techniques, such as electric probes and microwave interferometry. However, the small scale, strong laser absorption, stray light, plasma gradients, and multiple ion species in the higher density plasma are a significant experimental challenge.

1.7 Aim of the research

Characteristics of the DBD plasmas which are usually produced between parallel plane electrodes have not yet been understood well that is because diagnostics of micro discharges forming the DBD plasma are very difficult due to their short life times and small size. In order to assist understanding of DBD plasmas characteristics such as electron density and electron temperature, we are going to develop laser Thomson scattering (LTS) as a diagnostic method. In this system we have the light source that is second harmonics beam of the Nd: YAG Laser. When the YAG laser is injected into DBD plasma, Thomson scattered light is radiated from the electron. The local electron temperature and electron density in DBD plasmas are measured by the spectroscopic analysis of the Thomson scattering spectrum.

As a first step of the research, we will try to apply LTS to short pulsed discharges at around atmospheric pressure. Capacity coupled discharge (CCD) plasmas can be used as a first target of the measurement, because they can be produced at a desired position and at a predictable time. Usual DBD plasmas are not suitable for LTS measurements because it is difficult to produce DBD plasmas at a fixed position and at a fixed time. First, we must develop an electrode pair which can resolve this problem. The total electric charge which flows during the discharge period can be adjusted by choosing the capacitance of the capacitor. As a function of the capacitance, basic structures of atmospheric discharge plasmas can be studied at this stage.

The next step is development of discharge electrodes which can be compatible with LTS measurements. Then we execute LTS measurements to measure spatiotemporal evolution of electron density and electron temperature.

Finally, we apply LTS method at the early stage of the breakdown which is called streamer. Due to low electron density in streamer and small Thomson scattering cross section which lead to the weak scattering signal level, we must develop LTS method in this plasma new phase. In this case, we consider power density and energy of the laser probe and also employ photon counting detection technique to obtain a high signal to noise ratio.

References

[1] A. Schutze, The Atmoshperic-Pressure Plasma Jet: A Review and Comparison to Other Plasma Sources, IEEE Transactions on Plasma Science, 26, No.6, 1685 (1998).

[2] U. Kogelschatz, Dielectric Barrier Discharges: Their History, Discharge Physics, and Industrial Applications, Plasma Chemistry and Plasma Processing, 23, No. 1, 1 (2003).

[3] C. Tendero, Atmospheric Pressure plasmas: A Review, Spectrochimica Acta Part B, 61, 2 (2005).

[4] V. Gibalov, the Development of Dielectric Barrier Discharges in Gas Gaps and On Surfaces, J. phys. D: Appl. Phys. 33, 2618 (2000).

[5] I. Radu, Dielectric Barrier Discharges in Helium at Atmospheric Pressure: Experiments and Model in the Needle-Plane Geometry, J. Phys. D: appl. Phys. 36, 1284 (2003).

[6] V. Gibalov, Dynamics of Dielectric Barrier Discharges in Coplanar Arrangements, J. phys. D: Appl. Phys. 37, 2082 (2004).

[7] V. Gibalov, Properties of Dielectric Barrier Discharges in Extended Coplanar Electrode Systems, J. phys. D: Appl. Phys. 37, 2093 (2004).

[8] U. Kogelschatz, From Ozone Generators to Flat Television Screens: History and Future Potential of Dielectric Barrier Discharges, Pure Appl. Chem. Vol. 71, No.10, 1819 (1999).

[9] A. Chirokov, Atmospheric pressure Plasma of dielectric Barrier Discharges, Pure Appl. Chem. Vol. 77, No.2, 487 (2005).

[10] D.Trunec, Experimental Study of Atmospheric Pressure Glow Discharge, Contrib. Plasma Phys. 38, 3, 435 (1998).

[11] I. Muller, Self-Organized Filaments in Dielectric Barrier Glow Discharges, IEEE Transactions on Plasma Science, Vol. 27, No. 1, 20 (1999).

[12] B. Pashaie, Experimental Investigation of Micro-discharges in a Dielectric Barrier Discharge, IEEE Transactions on Plasma Science, Vol. 27, No. 1, 22 (1999).

[13] D. Trunec, Atmospheric Pressure Glow Discharge in Neon, J. Phys. D: Appl. Phys. 34, 1697 (2001).

[14] E. G. Finantu-Dinu, Development of Pulsed Surface Dielectric Barrier Discharge in Helium, IEEE Transactions on Plasma Science, Vol. 33, No. 2, 288 (2005).

[15] S. Celestin, Patterns of Plasma Filaments Propagating on a Dielectric Surface, IEEE Transactions on Plasma Science, Vol. 36, No. 4, 1326 (2008).

[16] A. Gleizes, Thermal Plasma Modeling, J. Phys. D: Appl. Phys. 38, R153 (2005).

[17] E.A.H. Timmermans, J. Jonkers, I.A.J. Thomas, A. Rodero, M.C. Quintero, A. Sola, A. Gamero, J. A. M. van der Mullen, The behavior of molecules in microwave-induced plasmas studied by optical emission spectroscopy. 1. Plasmas at atmospheric pressure, Spectrochimica Acta Part B, Vol. 53, 1553 (1998).

[18] C. Aragon, J. A. Aguilera, Characterization of laser induced plasmas by optical emission spectroscopy: A review of experiments and methods, Spectrochimica Acta Part B, Vol. 63, 893 (2008).

[19] Peackock N J, Robinson D C, Forest M J, Wilcock P and Sannikov V V, Nature, Vol. 224, 488 (1969).

[20] K. Uchino, T. Muraoka, K. Muraoka and M. Akazaki, Studies of an impulse breakdown

process in an atmospheric air using Ruby-laser scattering diagnostics, Jpn. J. Appl. Phys. 21, L696 (1982).

[21] Bowden M D, Okamoto T, Kimura F, Muta H, Ucino K, Muraoka K, Sakoda T, Maeda M, Manabe Y, Kitagawa M, and Kimura T, J. Appl. Phys. **73,** 2732 (1993).

[22] Cronrath W, Bowden M D, Uchino K, Muraoka K, Muta H and Yoshida M J. Appl. Phys. 81, 2105 (1997).

[23] Hori T, Bowden M D, Uchino K, Muraoka K, and Maeda M J. Vac. Sci. Technol. A, 14, 144 (1996)

[24] Hori T, Bowden M D, Uchino K, and Muraoka K. Appl. Phys. Lett. 69, 3683 (1996).

[25] Hori T, Bowden M D, Uchino K, and Muraoka K, J. Appl. Phys. 83, 1909 (1998).

[26] Sakoda T, Iwamiya H, Uchino K, Muraoka K, Itoh M and Uchida T, Japan. J. Appl. Phys. 36, L67 (1997).

[27] Wesseling H J and Cronrast B, J. Phys. D: Appl. Phys. 29 1035 (1996).

[28] Y. Noguchi, A. Matsuoka, M. D. Bowden, K. Uchino and K. Muraoka, Measurements of electron temperature and density for a micro-discharge plasma using laser Thomson scattering, Jpn, J. Appl. Phys., 40, 326 (2001).

[29] S. Hassaballa, M. Yakushiji, Y. K. Kim, K. Tomita, K. Uchino, and K. Muraoka: IEEE Trans. Plasma Science, 32, 127 (2004).

[30] S. Hassaballa, K. Tomita, Y.K. Kim, K. Uchino, H. Hatanaka, Y-M Kim, C-H Park and K. Muraoka, Jpn. J. Appl. Phys. 44, No. 14, L442 (2005).

[31] K. Muraoka, K. Uchino and M.D. Bowden, diagnostics of low-density glow discharge

plasmas using Thomson scattering, Plasma Phys. Control. Fusion, 40, 1221 (1998).

[32] K Muraoka, K Uchino, Y Yamagata, Y Noguchi, M Mansour, P Suanpoot, S Narishige and M Noguchi, Laser Thomson scattering studies of glow discharge plasmas, Plasma Sources Sci. Technol. 11 A143, (2002).

[33] Kelly Warner, Gary M. Hieftje, Thomson scattering from analytical plasmas, Spectrochimica Acta Part B, 57, 201 (2002).

Chapter 2

Laser Thomson scattering technique for non-thermal atmospheric pressure plasmas

2.1 Introduction

As mentioned in previous chapter, the knowledge of the electrons is important to evaluate possible mechanisms such as excitation and ionization mechanisms, including electron impact and radiative recombination, and in a more indirect manner, charge transfer and Penning ionization. The electron density and electron temperature also effect the electrical conductivity, thermal conductivity and viscosity of the plasma as well as they play key role in ambipolar diffusion. Thomson scattering determine the electron properties in discharge plasmas. The electromagnetic radiation of a laser beam incident on plasma, and forces the free electrons in the plasma to oscillate and induces them to radiate light. Since the electrons move rapidly with respect to both the laser beam and the detector, the resulting Thomson scattering signal is broadened due to Doppler effect.

2.2 Laser-plasma interaction

When a laser beam is injected into a plasma, the laser radiation scatters non-resonantly from free and bound electrons in the discharge. The total spectrum of scattered light contains three main components: (1) Thomson scattering component which emerges from scattering by free electrons. (2) Rayleigh scattering component which arises from incoherent scattering from the bound electrons in the atoms and ions. (3) Stray light component which appears from laser radiation scattering by the surfaces and windows of the chamber. The Thomson and Rayleigh scattering, which are both Doppler-broadening due to motion of the scattering particles, have different spectral widths due to the much higher velocity of the electrons compared with the atoms ions. A schematic of scattering spectrum is shown in Fig. 2.1.
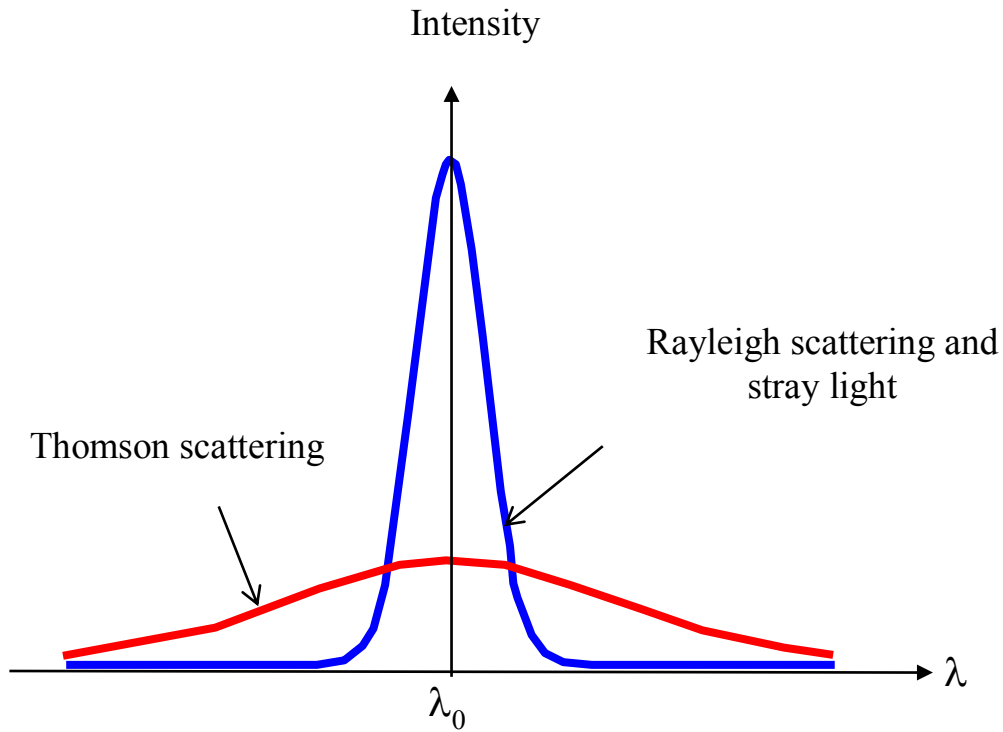
Fig. 2.1 Different components of the total scattered spectrum

2.2.1 Principle of Thomson scattering

When the electromagnetic radiation of an incident laser beam interacts with a charged particle in a plasma, the oscillating field of the radiation induces the charge to oscillate in resonance with the field. The oscillating charge radiates light which is called Thomson scattering. Since the radiating charges are moving rapidly with respect to both the laser beam and detector device, the wavelength of scattered radiation that reaches a detector is doubly Doppler shifted. The wave

length of scattered light will be a function of the velocity component of the charge along the differential scattering wave vector, **K**, which is defined as the vector difference between the wave vector of the scattered light, **K$_s$**, and the wave vector of the incident laser beam, **K$_i$**.

$$\mathbf{K=K_s - K_i} \qquad\qquad (1)$$

Figure 2.2 shows the relationship among these wave vectors. The magnitude of K is a function of the laser wavelength λ_i, and the detection angle θ between scattered vector K$_s$ and incident vector K$_i$. In the non-relativistic condition, the velocity of the scattered particle is small compared to the speed of light. So it can be assumed that the wavelength of scattered radiation and incident radiation are approximately the same.

$$K = 2K_i \, sin\left(\frac{\theta}{2}\right) = \frac{4\pi}{\lambda} sin\left(\frac{\theta}{2}\right) \qquad\qquad (2)$$

The Doppler shift of the scattered radiation $\Delta\lambda$ can be written as follows:

$$\Delta\lambda = \lambda - \lambda_i = -\frac{(\mathbf{K}.v)\lambda_i^2}{2\pi c} \qquad\qquad (3)$$

Where λ_i is the wavelength of the incident laser beam, v is the velocity of the particle, λ is the scattered wavelength, and c is the speed of the light. This equation shows the dependent parameters of the Doppler-broadened Thomson spectrum.
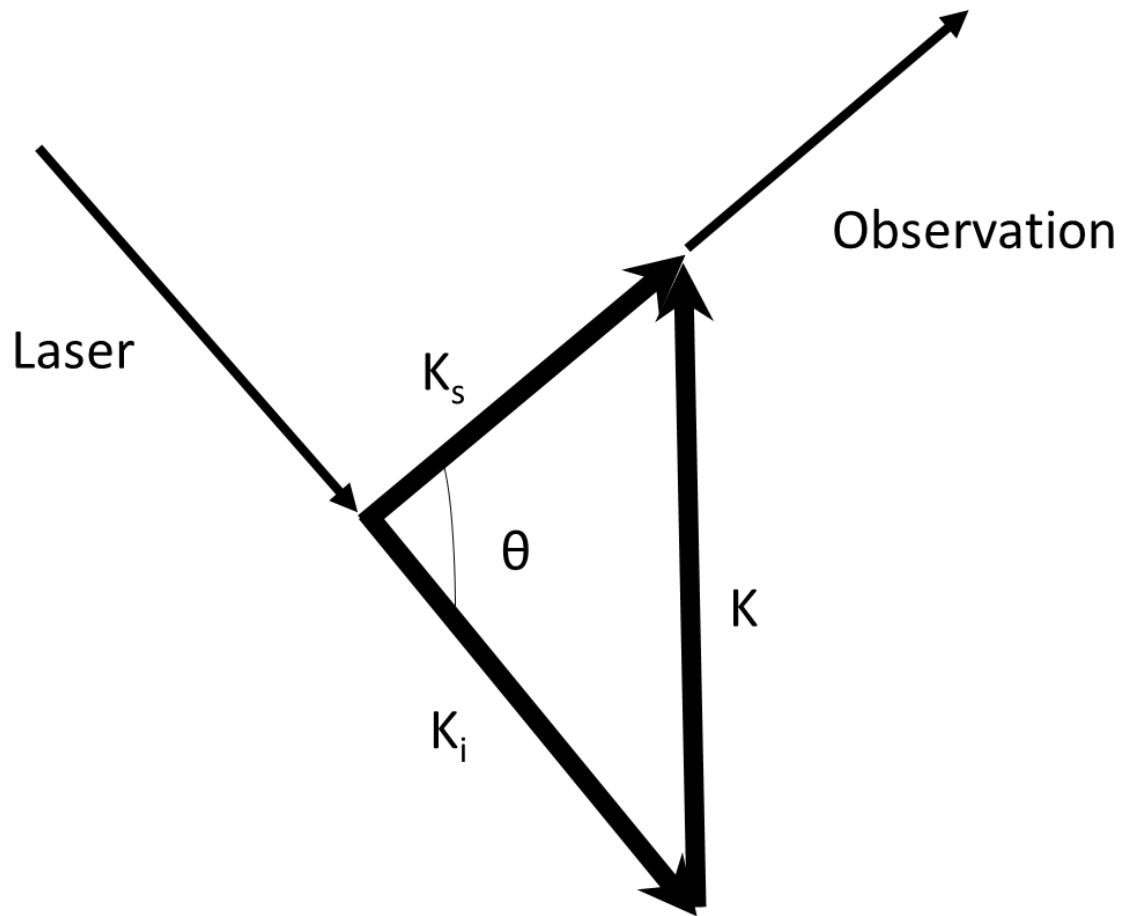
Fig. 2.2 The relation among the wave vector of the incident laser beam K_i, the vector along the observation direction K_s, and the differential scattering wave vector K.

Charges with velocities parallel to **K** scatter light with the maximum wavelength shift. Because they are moving in the same direction relative to both the laser and the detector. On the contrary, those charges moving perpendicular to **K**, will scatter light wavelength equal to laser wavelength. Because the Doppler shifts with respect to the laser and detector cancel each other. Based on the eqs. 2 and 3, the wavelength shift is minimized and maximized at θ=0 and θ=180,

respectively. Also larger Doppler shifts are obtained with longer wavelength lasers. So broader spectrum can be achieved larger by choosing laser wavelengths and angles.

The most important parameters that govern the shape of a Thomson scattering spectrum are the differential scattering wave vector and the Debye length. These two parameters have been combined to define the scattering parameter which is called α:

$$\alpha = \frac{1}{k\lambda} = \frac{\lambda_i}{sin\left(\frac{\theta}{2}\right)}\left(\frac{n_e e^2}{4\pi k_B T_e}\right) \qquad (4)$$

The value of α determines the character of the scattering which is observed in an experiment. It is clearly depend on the laser wavelength, electron temperature, electron density, and scattering geometry. Based on α, there are three scattering regimes. If the wavelength associated with the scattering wave vector is equal to or greater than the Debye length, so that α ≥1, then the incident laser beam interacts with the shielded charges what is known as coherent scattering. Conversely, if the scattering wavelength is smaller than Debye length (α ≤ 0.1), then the incident wave interact to charges individually, producing incoherent scattering. On the other hand, the range in which 0.1≤ α ≤1.5 is a transition region between the two regimes of coherent and incoherent scattering. These different scattering regimes produce different spectra. So the value of α in a specific experiment should be considered always when data are interpreted. For example, for α ≥1 the scattering is insensitive to the electron energy distribution [1]. The value of α is determined from the mean velocity of the bulk of the electrons, so information about electron energy distribution function (EEDF) cannot be obtained at large value of α. At intermediate value of α, approximately α=1, the shape of the spectrum is affected by both electron density and electron temperature. Therefore, by fitting the spectrum to theoretical curves and both electron density and electron temperature can be calculated from the spectral shape [2]. Finally, by assuming that α is much smaller than 1 and the electron energy distribution is Maxwellian, it provides a very convenient method for determining electron temperature.

The total scattered power induced by an incident laser beam can be expressed relatively. If a beam of radiant power P_I and cross sectional area A interacts with a plasma over a length L, and if the density of particles in this area of the plasma is n, then the beam will interact to the volume (V) with a total number of particles (N) as follows:

$N=nV=nAL$ (5)

The cross section of each particles is σ, then N particles have a total cross section of $nAL\sigma$. Therefore, in the case of a plasma medium, the fraction of the cross section that is filled with particles, and the fraction of photons that are scattered is:

$$f = \frac{nAL\sigma}{A} = nL\sigma \qquad (6)$$

And the scattered power is:

$$P_s = P_1 nL\sigma \qquad (7)$$

The interaction between an electron and a photon induces the electron to oscillate as dipole, so the Thomson scattering cross section and the scattered power is not isotropic. This cross section can be written as follows:

$$\frac{d\sigma_T}{d\Omega} = \left(\frac{e^2}{m_e c^2}\right)^2 sin^2(\vartheta) \qquad (8)$$

where ϑ is the polar angle between the polarization direction of the laser beam and the detected scattered light direction. The angle ϑ can also be written as follows:

$$\vartheta = |\hat{s} \times (\hat{s} \times \hat{e})| \qquad (9)$$

where $\hat{s}$ is the unit vector corresponding to the scattered light, pointed from the detection volume to the detector, and $\hat{e}$ is the unit vector directed along the laser electric field direction. Fig. 2.3 shows the relative orientations of the laser beam, the scattering, and the detector. The directional dependence determine the effect of the laser beam polarization on the observed scattering signal. The maximum value of the cross product, and the strongest scattered signal, will obtained from an electric field polarized perpendicular to the plane defined by the laser beam and the observation direction.
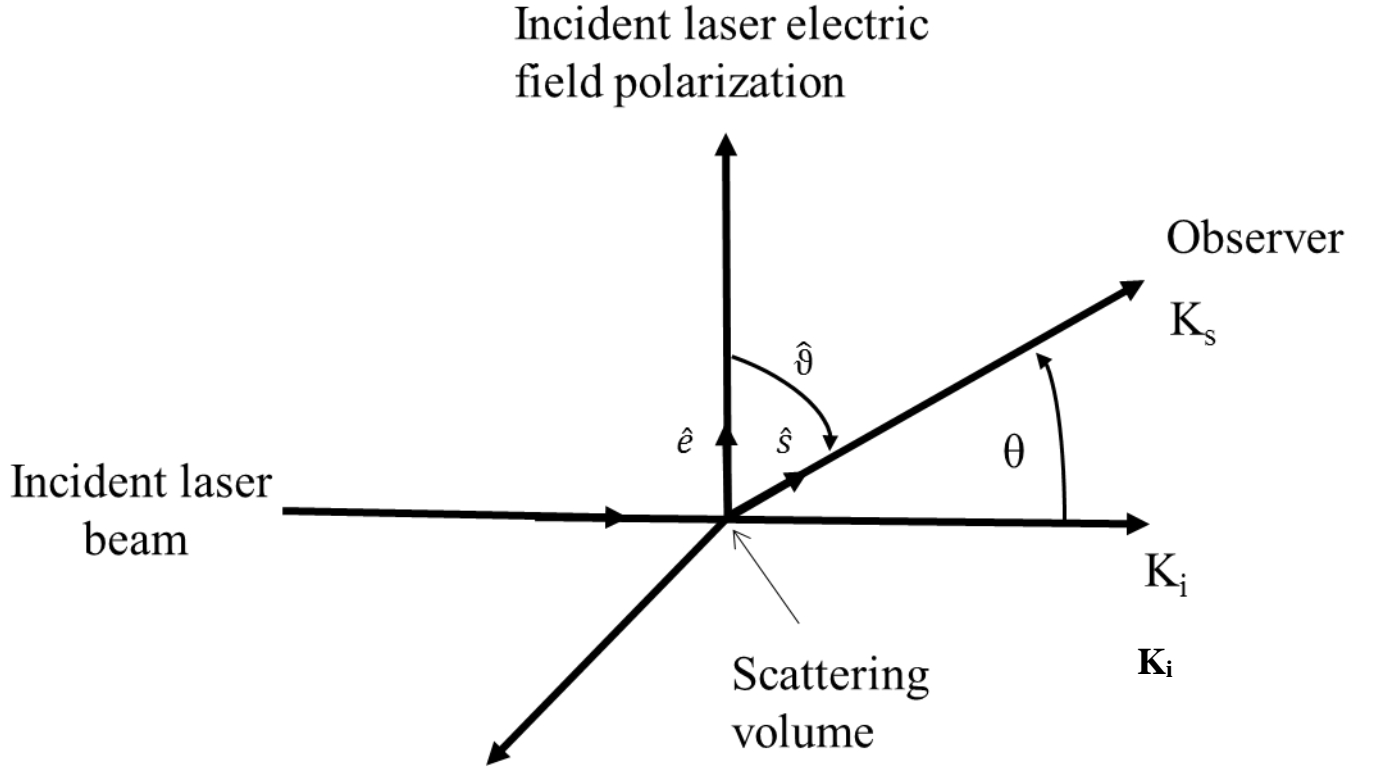
Fig. 2.3 the spatial relationship between the laser beam, the electric field polarization, and the
detector.

By integrating over the entire solid angle, the value of the Thomson cross section calculated to be:

$$\int \frac{d\sigma_T}{d\Omega} d\Omega = \sigma_T = \frac{8\pi e^4}{3m_e^2 c^4} = 6.653 \times 10^{-25} cm^2 \qquad (10)$$

The calculation shows that the Thomson scattering cross section is extremely small, consequently the signal intensity of scattering is too weak. Eqs. 7 and 10 show that even in experiments with high powered lasers, due to low electron number densities, it might be difficult to probe using Thomson scattering.

Introducing the value and directional dependence of σ_T and the frequency dependence of P_s, the scattered power in solid angle $d\Omega$ and within a frequency range $d\omega$ induced by the electric field of incident laser beam of power P_1 can be written as follows [3]:

$$P_s d\Omega d\omega = \frac{P_1 n_e L e^4}{2\pi m_e^2 c^4} d\Omega d\omega |\hat{s} \times (\hat{s} \times \hat{e})|^2 S(K, \omega) \qquad (11)$$

Where L is the interacting length between the laser and the plasma viewed by the detector, $\hat{s}$ is the unit vector pointed from the detection volume to the detector, $\hat{e}$ is the unit vector directed along the laser electric field, and S($\mathbf{k}$,ω) is the spectral density function which reflects the spectral distribution of the scattered photons. This function which conveys the density of ions and electrons in the plasma, is a function of k, α, ω, electron temperature and ion temperature. The ion scattering is not included in this scattered power expression because of the mass dependence of the scattered power. Ions are too massive to be accelerated by laser. So they do not radiate detectable scattering. The expression also assumes that the electrons motion is non-relativistic which allows the Lorentz force of the laser magnetic field on the free electrons to be neglected.

The spectral density function shows the shape of the Thomson scattering spectrum which is defined by fluctuations in local electron density or motion. The function S($\mathbf{k}$,ω) is an autocorrelation of these fluctuations as a function of the wave vector and frequency. The detailed derivations of the function can also be found in ref. [3]. The function reflects the fact that shielding due to both ions and electrons affects Thomson scattering from electrons at large values of α. Also, due to the big difference in mass of ions and electrons, scattering due to electrons shielded by ions would occur at very different velocity shifts than electrons shielded by the other electrons. In this case, the expression can be separated into an ion term and an electron term as long as the electron temperature is not much greater than the ion temperature. It causes the analysis of the scattering spectra to be much more convenient. By assuming that the plasma is collisionless (the collision frequency is less than plasma frequency) and distribution functions of electron and ion are both Maxwellian, the function can be written as follows [4, 5]:

$$S(\mathbf{k}, \omega) = |\frac{1}{1+\alpha^2 W(\chi_e)}|^2 \frac{\exp(-\chi_e^2)}{\pi^{\frac{1}{2}}} d\chi_e + Z(\frac{\alpha^2}{1+\alpha^2})^2 |\frac{1}{1+\beta^2 W(\chi_i)}|^2 \frac{\exp(-\chi_i^2)}{\pi^{\frac{1}{2}}} d\chi_i = \Gamma_\alpha(\chi_e) d\chi_e +$$

$$Z(\frac{\alpha^2}{1+\alpha^2})^2 \Gamma_\beta(\chi_i) d\chi_i \qquad (12)$$

where

$$\chi_e = \frac{\omega}{kv_e}, \quad \chi_i = \frac{\omega}{kv_i}, \quad \beta^2 = Z\frac{\alpha^2}{1+\alpha^2}\frac{T_e}{T_i} \tag{13}$$

$$\Gamma_\alpha(\chi_e) = \frac{\exp(-\chi_e^2)}{|1+\alpha^2 W(\chi_e)|^2 \pi^{1/2}}$$

$$\Gamma_\beta(\chi_i) = \frac{\exp(-\chi_i^2)}{|1+\beta^2 W(\chi_i)|^2 \pi^{1/2}} \tag{14}$$

$$W(\chi) = 1 - 2\chi e^{-\chi^2}\int_0^\chi e^{\chi^2}dP - i\pi^{1/2}\chi e^{-\chi^2} \tag{15}$$

The index of χ in eq. (15) can be (e) or (i). Also the mean thermal speed of the electron and ion are as follows:

$$v_e = \left(\frac{2k_B T_e}{m_e}\right)^{1/2}, \quad v_i = \left(\frac{2k_B T_i}{m_i}\right)^{1/2} \tag{16}$$

In above equations, Z is the charge number of the ion, T_i is the ion temperature, and m_i is the ion mass. The first term in eq. (12) is the electron term, and second one is the ion term. By integrating eq. (12) over frequency ω the equation becomes as follows [2]:

$$\int S(\mathbf{k}, \omega)\frac{d\omega}{2\pi} = S_e(\mathbf{k}) + S_i(\mathbf{K}) \tag{17}$$

Where

$$S_e(\mathbf{k}) = \frac{1}{1+\alpha^2} \tag{18}$$

$$S_i(\mathbf{k}) = \frac{Z\alpha^4}{(1+\alpha^2)(1+\alpha^2+Z\left(\frac{T_e}{T_i}\right)\alpha^2)} \tag{19}$$

It can be seen by these two equations the electron feature has a total intensity that depends on the parameter α merely with a frequency spread that is function of T_e. The same explanation can be said for ion term. When α is much smaller than 1, the ion terms in both eqs. (12) and (17) become approximately zero. In this case, scattering is on the scale of individual electrons, so shielding by both electrons and ions can be neglected and the shape of the spectrum reflects the electron velocity distribution. The expression for the scattered power based on the eqs. (11) and (12) after conversion from frequency to wavelength units can be written as follows:

$$P_s d\Omega d\lambda = \frac{P_1 n_e L e^4}{2\lambda_0 v_e \pi^{1/2} m_e^2 c^3 \sin(\frac{\theta}{2})} d\Omega d\lambda |\hat{s} \times (\hat{s} \times \hat{e})|^2 \exp(\frac{-c^2 \Delta\lambda^2}{4v_0^2 \lambda_0^2 \sin^2(\frac{\theta}{2})}) \qquad (20)$$

2.2.1.1 Electron temperature

The exponential term in eq. (20), reflects the Gaussian shape of a Maxwellian electron energy distribution. In fact, when the electron velocity distribution function is Maxwellian, the Thomson scattered spectrum is Gaussian in shape. This term depends on T_e for a particular experimental design, so it can be used to drive the electron temperature form spectrum. Taking the natural logarithm of both sides of eq. (20) yields:

$$\ln(P_s) = \frac{-c^2 m_e}{8k_B T_e \lambda_0^2 \sin^2(\frac{\theta}{2})} \Delta\lambda^2 + cte \qquad (21)$$

where T_e is in eV and λ_0 and $\Delta\lambda$ are in the same units. Therefore, by plotting the natural log of the Thomson scattering intensity as a function of the wavelength square, the electron temperature can be derived from the slop of the line.

For example, by considering the slop of the line is A, the perpendicular angle of Thomson scattering experimental setup ($\theta = \pi/2$), and the incident laser wavelength of 532 nm, the electron temperature in term of eV can be calculated as:

$$T_e = \frac{0.456}{A} \qquad (22)$$

2.2.1.2 Electron density

The electron density (n_e) is proportional to the total intensity of the scattered signal directly. It can be obtained from normalized magnitude of the spectrum integrated over the whole wavelength rang. Thus, n_e can be determined from the measured spectrum if the absolute sensitivity of the detection system is calibrated accurately. This calibration is easily done by measuring the Rayleigh scattered intensity when the chamber is filled with gas at operated pressure without plasma. In fact, the most convenient method for calibration employs Rayleigh scattering. Rayleigh scattering produces a signal at the laser wavelength, as a result of scattering from gas atoms. This signal is not significantly Doppler broadened because the atoms in the plasma are moving much more slowly than the electrons. The intensity of Rayleigh scattering from a known density of gas, like that of Thomson scattering, is dependent on the laser power,

the number density, and cross section of the scattering. In this case, the scattered signal intensities from a plasma with unknown electron density n_e (I_p) and from a gas with known density n_0 (I_g) are given by these two following eqs. :

$$I_p = n_e \sigma_{Th} \Delta\lambda_p f_{sys} \qquad (23)$$

$$I_g = n_0 \sigma_R \Delta\lambda_g f_{sys} \qquad (24)$$

in which σ_{Th} and σ_R are differential cross sections for Thomson scattering and Rayleigh scattering, respectively. Also $\Delta\lambda_p$ and $\Delta\lambda_g$ are the spectral widths of the scattered spectra from the plasma and the gas, and f_{sys} is a function of the laser energy and the efficiency of the detection system. Since both measurements are made using and the same laser and detection systems, f_{sys} is the same, so the electron density can be calculated as follows:

$$N_e = N_0 \frac{I_p}{I_g} \frac{\sigma_R}{\sigma_{Th}} \frac{\Delta\lambda_g}{\Delta\lambda_p} \qquad (25)$$

Actually, the spectral widths of the measured spectra are convolutions of the true scattered spectra (Thomson and Rayleigh) and the instrument function of the spectrometer used to measure the spectra. Since the actual Rayleigh width is extremely small, the width of the measured gas spectrum simply equals to the width of the instrument function of the spectrometer [6].

2.2.2 Rayleigh scattering

Elastic scattering of photons by heavy particles is called Rayleigh scattering. In this process, the particles do not gain or loss internal energy. It is well known that Rayleigh scattering occurs when the size of the particles is considerably smaller than the wavelength of probing radiation. The Rayleigh scattering signal is proportional to the density of heavy particles (n). By applying the ideal gas law $P = n_h k_B T_g$, the heavy particle density is inversely proportional to the gas temperature T_g at constant given pressure P.

The differential cross section $\frac{d\sigma_{rayleigh}}{d\Omega}$ for Rayleigh scattering depends on the species, which means that the measurement should be done with the same gas composition. However, in some gas species the cross sections for Rayleigh scattering are very similar. For example, the cross

section of argon and air are very similar: $5.4 \times 10^{-32}\,\text{m}^2$ for argon versus $6.2 \times 10^{-32}\,\text{m}^2$ and $5.3 \times 10^{-32}\,\text{m}^2$ for nitrogen and oxygen, respectively [7-9].

2.2.3 Raman scattering

Inelastic scattering by molecules, which can undergo a rotational or vibrational transition, is referred to as Raman scattering. In this process, the internal energy (rotational and vibrational) of the molecules change that it lead to specific wavelength shifts of the scattered photons. In Raman scattering the scattered photon $h\upsilon_s$ has different energy than the incident photon $h\upsilon_i$. Those photons which have lost energy to the molecule form stoke lines and those photons which have gained energy from molecule form Anti-Stoke lines, as can be seen in Fig. 2.4 [9, 10].

$$h\upsilon_i + \text{M}(\text{E}_i) \longrightarrow \text{M}^*(\text{E}_f) + h\upsilon_s \qquad (26)$$

$$h\upsilon_i - h\upsilon_s = \text{E}_f - \text{E}_i > 0 \qquad \text{Stokes lines} \qquad (27)$$

$$h\upsilon_i - h\upsilon_s = \text{E}_f - \text{E}_i < 0 \qquad \text{Anti-stokes lines} \qquad (28)$$
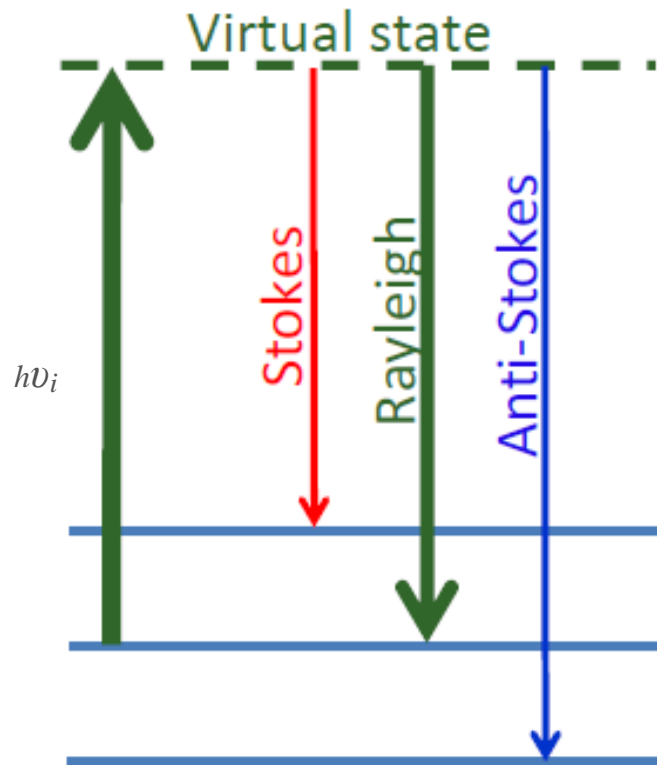
Fig. 2.4 Schematic view of the Raman scattering

2.2.4 Laser perturbation in plasma

The advantage that the laser is said to have over probe techniques as a plasma diagnostics method is that there is no way perturbs the plasma whose properties are being measured. However, it is clear that the concentration of an intense laser beam into a plasma can probably

influence the plasma`s electron temperature and density, so it gives the measured value of these parameters unreliable. Two kinds of perturbation effect can be distinguished. The first one is simple heating of the plasma local to the laser beam by absorbing beam radiation. The second one is that the laser beam can increase the ionization degree and electron density by direct photo-ionization or multi-photon process.

The electrons in the plasmas can be heated by electric field of the intense laser beam. Heating of the plasma can be treated as occurring through the process of inverse bremsstrahlung, which is the absorption of the photon by an electron near a heavy ion.

Assuming the electron-electron relaxation time is short compared to the length of the laser pulse, radiation absorbed by inverse bremsstrahlung can be regarded as increasing the electron temperature in plasma during the laser pulse. The fractional increase in electron temperature has been estimated by Kunze (1965) [11, 12]. The increase in electron temperature can occur under these conditions and under the further assumption that heat has not been much conducted away during the time of the pulse. The formula for the fractional increase is as follows:

$$\frac{\Delta T_e}{T_e} = 5.32 \times 10^{-7} \left(\frac{nZ}{T_e^{\frac{3}{2}}} \right) \lambda^3 \left(1 - \exp\left(-\frac{h\upsilon}{T_e}\right)\right) I_0 \Delta\tau \qquad (29)$$

where n is the electron density in cm^{-3}, Ze is the charge on the ions, T_e is electron temperature in eV, λ is wavelength of the laser light in cm, I_0 is laser intensity in W/cm^2, and $\Delta\tau$ is laser pulse length in seconds. The $h\upsilon$ in exponential expression is photon energy associated with laser emission.

In addition to heating the plasma, laser beam can perturb the plasma by direct photo-ionization or multi-photon processes. Direct ionization only occur for the excited atomic states that are less than 2.33 eV below the continuum (for laser beam 532 nm). The cross sections of multi-photon processes are much smaller than that of direct photo-ionization, but multi-photon processes may become important at very high laser irradiations [13].

2.3 Application of laser Thomson scattering to non-thermal atmospheric pressure micro discharge plasmas

Thomson scattering diagnostics for measurements of electron density and electron temperature in atmospheric pressure discharge plasmas have been developed in our laboratory for more than ten years [14, 15]. The LTS measurements have also been reported by another research group [16]. In general, micro discharge plasmas are characterized by small volume, limited spatial extension of the discharge, and the relatively high pressure levels of the gas in the discharge. Therefore, to apply LTS to micro-discharge plasmas, it is so important to consider these special features of the micro-discharge plasmas on the LTS experiment design. The small discharge volume results in a small scattering volume. Consequently, it leads to small Thomson scattering signal. Due to limited spatial extension of the discharge and the need to perform the LTS measurement extremely close the electrode, increase the intensities of the stray light signal level. Also because of the relatively high pressure levels applied in micro-discharge plasmas and the low degree of ionization, the neutral densities are several orders of magnitude higher than the electron density. It increases the intensity of Rayleigh scattering signal which may overwhelm Thomson scattering signals. Another problem is the possibility of perturbing the discharges by the laser probe. To solve the above mentioned challenges, we discuss in more details about experimental arrangements as well as outline the structure of streamer and micro discharge.

2.3.1 Streamer and micro-discharges in atmospheric-pressure

Generally, the Townsend breakdown mechanism can be applied only for relatively low pressures and short gaps (pd < 40 Torr.m at atmospheric pressure d < 0.05 m). Another breakdown mechanism called streamer which happen in larger gaps at high pressures. The streamer provides breakdown in a local narrow channel. Streamers are also primarily related to avalanches, but in large gaps the avalanches cannot be considered independently. A streamer is a thin ionized channel that rapidly propagates between electrodes by an intensive primary avalanche. This avalanche also generates photons which launch numerous secondary avalanches in near the primary one. Electrons of the secondary avalanches are pulled by the strong electric field into the positively charged trail of the primarily avalanche, creating the rapidly propagating streamer between electrodes [20].

As avalanche propagation, the primary electrons drift to the anode, ionizing the gas and generating avalanches. The ionization in avalanches is usually described by Townsend ionization coefficient α, indicating the number of produced electrons per unit length along electric field:

$$\frac{dn_e}{dx} = \alpha n_e \qquad (1)$$

The total number of produced electrons equal to:

$$n_e = n_{e0} exp(\alpha x) \qquad (2)$$

As shown in eq. (2), number of electrons in avalanche grows exponentially with distance traveled by avalanche and ionization coefficient that depend on the electric field. Since collision rates is high at atmospheric pressure, electron avalanche can grow up and generate considerable charge density at its tip, already after traveling a short distance. The qualitative change happen when the charge amplification in the avalanche exp (αx) becomes large and create space charge that it leads to appreciable electric field which should be added to the external one. The electrons are in the head of the avalanche while the positive ions remain behind that form an electrical dipole. The local electric field due to charge separation resulting from the difference in drift velocities of electrons and ions is superposed on the applied electric field. In front of the avalanche head the applied and local electric fields add up to make a stronger electric field which boost ionization process. On the contrary, inside the avalanche, the total electric field is lower than the external one which slows down the ionization. Once the avalanche head reaches the anode, electrons flow into the electrode and it is mostly the ionic trail that remains in the gap.

Collisional ionization in the high electric field region at the avalanche head leads to fast propagation of the ionization region and the formation of a bright plasma channel which is called streamer. As a matter of fact, a strong primary avalanche is able to boost the external electric field and form a streamer. The avalanche to streamer transformation takes place when the internal field of an avalanche becomes comparable with the applied one. If the gap is short, the transformation happen only when the avalanche reaches the anode. Such a streamer that grows from anode to cathode called the cathode directed or positive streamer and vice versa, if the avalanche to streamer transformation can occur far from the anode, the anode directed or negative streamer grows toward both electrodes.

The streamer velocity is in the range of $10^5 - 10^6$ m/s, the radius of the propagating streamer head and the resulting ionized channel is about $10^{-4} - 10^{-3}$ m [21]. High energy photons emitted from the primary avalanche provide photo-ionization in the vicinity, which form the secondary

avalanches. Electrons of the secondary avalanches are pulled into the ionic trail of the primary one and create a quasi-neutral plasma channel. The cathode directed streamer starts near the anode, where the positive charge and electric field of the primary avalanche is the highest. The streamer looks like a thin conductive needle growing from anode. The plasma density in the streamer also corresponds to the maximum electron density in the head of the primary avalanche that is about $10^{18} - 10^{19}\,\mathrm{m^{-3}}$.

The measurements of region described in this research are shown in Fig. 1.1: 1) streamer 2) secondary streamer (in small scale is known as micro discharge). They are becoming the most commonly used plasma source for plasma processing applications used in plasma nano-science, plasma medicine, and plasma chemistry [17-21].

A strong primary avalanche is able to boost the external electric field and form a streamer. When the streamer channel connects the electrodes, the electrical current may be significantly increased to form secondary streamer or micro-discharge. In our research, we use positive streamer or cathode directed streamer. Such streamer grows from anode where the positive charge and electric field of the primary avalanche is the highest. The streamer looks like a thin conductive needle growing from the anode. The electric field at the tip of the anode needle is very high, which provides high energetic electrons and streamer growth velocities, about $10^5 - 10^6\,\mathrm{m/s}$. The streamer cross the gap in a few nanoseconds and forms a conducting channel of weakly ionized plasma. An intensive electron current flows through this plasma channel until the local electric field collapses. This collapse is caused by the charges accumulation on the dielectric surface. The collection of processes in the discharge gap initiated by avalanche and developed until electron current termination is called micro-discharge. Fig. 2.5 shows streamer propagation from anode to cathode while attracting additional avalanches. A micro discharge is formed by channel streamers that strike at the same place each time the polarity of applied voltage changes [20]. In the most of cases, dielectric barrier discharges are not uniform and contain enormous micro-discharges built from streamers and distribute in the discharge gap [19].
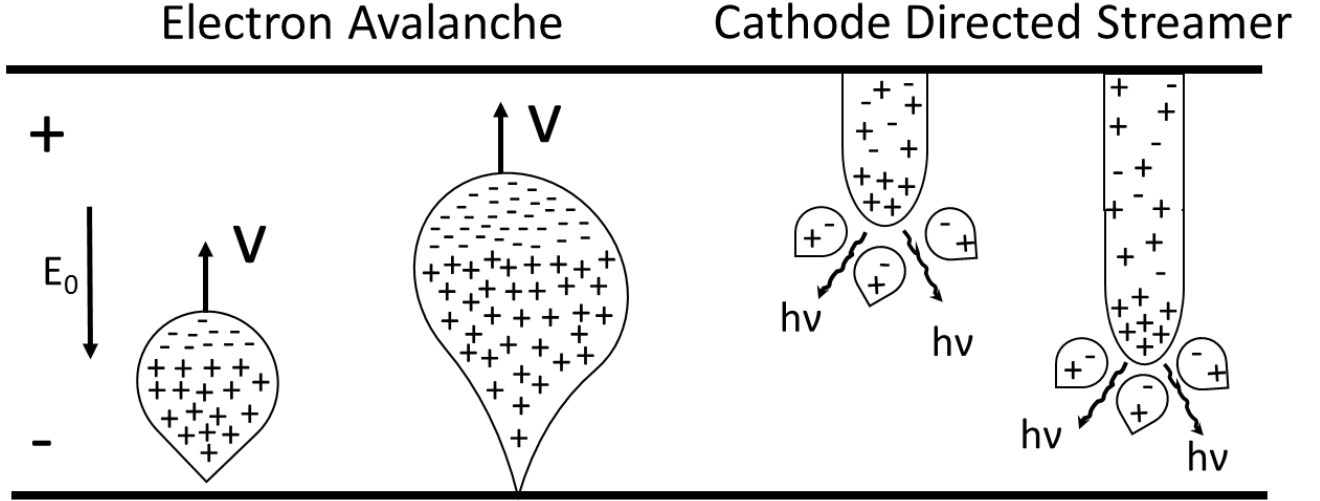
Fig. 2.5 Avalanche development, avalanche to streamer transition, and streamer propagation in
discharge gap.

2.3.2 Scattered signals and signal to noise level in micro-discharge plasmas

The main practical problem in measurement of the spectrum is that the cross section for scattering of radiation from electrons is extremely small, so the amount of scattered light is also extremely small, even when high intensity lasers are used as a light source. The total number of photo-electrons N_{pe} which should be detected in a scattering experiment can be estimated using following expression:

$$N_{pe} = \left(\frac{E_L}{h\upsilon}\right)\Delta V N_e \sigma_{Th} \Delta\Omega \tau_L \eta \varepsilon \qquad (30)$$

In this equation, E_L is the laser energy, h is the Planck's constant, υ is the laser frequency, ΔV is the scattering volume, $\Delta\Omega$ is the detection solid angle, τ_L is the pulse length of the laser, η is the transmission of the section system, and ε is the quantum efficiency of the detector used. The detected signal for a given electron density can be calculated using this expression.

For the case of the micro-discharge used in this study, laser energy E_L is 10 mJ, laser wavelength is 532 nm, beam diameter is 50 μm, the pulse length of the laser τ_L is 8ns, the scattering volume ΔV is defined in terms of multiplication of slit height (1mm) and slit width (0.1 mm) of the spectrometer, and spot size that is calculated to be $5 \times 10^{-12}\,\mathrm{m}^3$, $\eta = 0.1$, $\Delta\Omega = 0.13$ srad, and $\varepsilon = 0.35$. Assuming that the electron density in this study is in order of $10^{22}\,\mathrm{m}^{-3}$, the number of photoelectrons detected per laser pulse is estimated to be about 5000. This number of photoelectrons forms small signal. Even the number of photoelectrons in streamer phase decrease too much. In addition, the background emission of plasma in the region of the laser wavelength may be easily as large as this. The weak signals problem is overcome to some extend by averaging the detected signal over many laser pulses. This procedure can improve the measured signal to noise ratios greatly. By using this procedure, there is a disadvantage that random fluctuations in the discharge which happen over short time duration cannot be detected. The signal to noise ratio is determined by the relative sizes of the Thomson scattered signal and the background plasma emission. Usually signals are obtained by analogue mode; however, when the signals become too weak, photon counting methods can be used. In this case, the signal to noise ratio is as follows:

$$\mathrm{SN} = \frac{N_T}{\sqrt{N_T + N_E}} \qquad\qquad (31)$$

where N_T and N_E are the number of detected photo-electrons due to Thomson scattering and background emission, respectively. It should be noted that the signal to noise ratio depends on the amount of data which is averaged, and the other factors which determine N_T such as the laser energy, and other parameters in eq. 30.

2.3.3 Thomson scattering experimental system

As Fig. 2.6 shows, the plasmas source mount inside of a stainless steel chamber which is called discharge chamber. It contains several large glass windows for optical access. The laser beam enter and exit the chamber through Brewster windows, while a series of baffles on both the entrance and exit paths served to minimize the transmission of stray light due to scattering of the laser from the windows. The beam is injected perpendicular to the axis of the chamber and is focused by lens. The focal length determine spot size consequently determine spatial resolution. The Thomson scattered light is collected by a lens and directed into a triple grating spectrometer

(TGS). The entrance slit of TGS is oriented so that its longer side is parallel to the direction of the laser beam propagation. This feature enable the maximum amount of scattered light to enter the detection system.
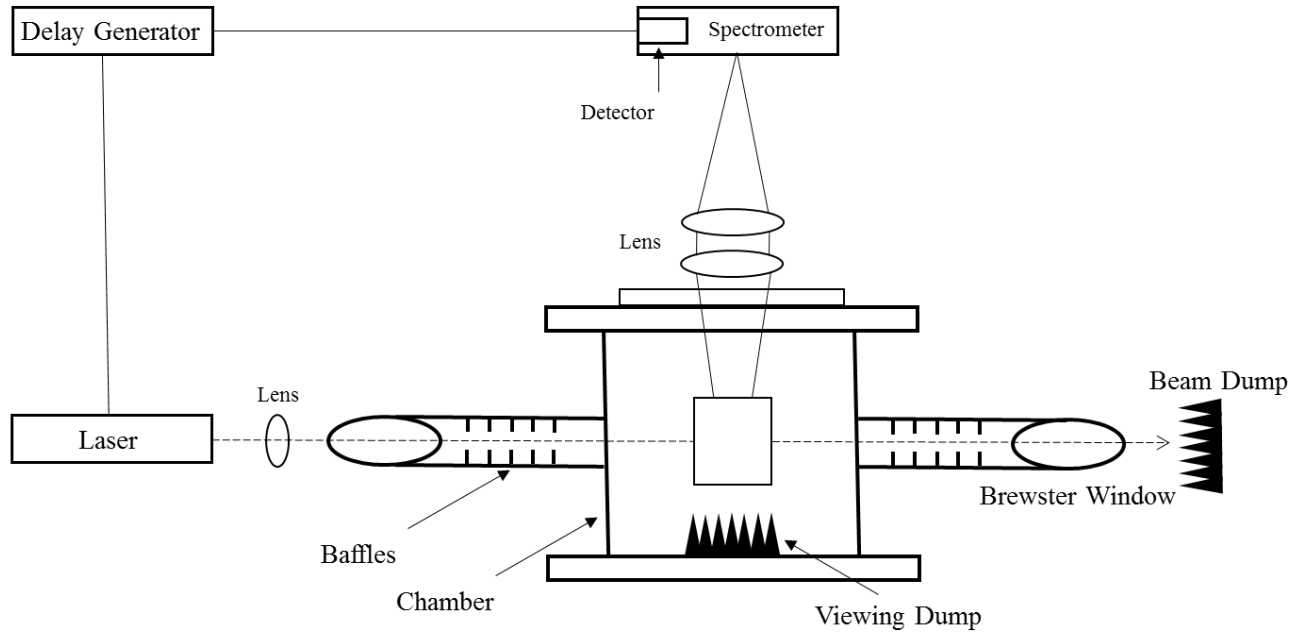
Fig. 2.6 Schematic of experimental arrangement for a laser Thomson scattering system

The output of the TGS is detected by an ICCD camera. The detection system is oriented to detect scattering from the plasma via window on the chamber. The entire detection system could be translated and rotated so that scattering could be observed from different radial position in the plasma. A small viewing dump is positioned so that the stray light is minimized.

As mentioned in previous section, one of the keys to the success of this kind of experiment is the accumulation of the scattering data which is necessary to overcome the problem of the

extremely small scattered signal from a single laser pulse. In addition to above main feature, desirable properties of good beam divergence, good quality beam profile and good reliability, the laser source should be able to be operated at a relatively high repetition rate at a relatively high energy per pulse. Moreover, the wavelength should be in the mid-visible range, where sensitive, low noise detectors are available. In high temperature plasmas a single-pulse ruby laser, with an energy 1 J per pulse was used initially as a natural extensions of experiences [22]. Measurements were made by accumulating data for ten laser pulses for each wavelength point of the measured spectrum. Based on this requirement, the YAG laser, operated at the second harmonic wavelength of 532nm, has been found to be the most suitable laser used up until now for Thomson scattering experiments in non-thermal atmospheric pressure plasmas.

A spectrometer which can disperse the measured spectrum sufficiently so that the Thomson scattering and Rayleigh scattering spectra can be separated is required. For these type of discharges which have electron temperature of few eV, the Thomson scattering spectrum with is typically 2-3 nm. The use of triple grating spectrometer (TGS) increases the rejection of stray light and Rayleigh scattering at wavelengths from the laser wavelength. The grating constants in our study is 1200 grooves/mm that is favorable since it results in the best dispersion, yielding the best spectral resolution and narrowest instrumental profile. This allows more accurate measurement of weak signals. In addition, using larger grating constants the focal length

As mentioned before, the signals in Thomson scattering experiment are usually weak, and this means that sensitive, low-noise detectors are essential. In old investigations, photomultipliers with quantum efficiency of between 10% and 20% was used [14, 15]. ICCD cameras with low noise, high gain, and quantum efficiencies of 35% are readily available and very reliable at present time in non-thermal atmospheric pressure plasmas.

To process the detected signals by ICCD camera, two different procedures are used. In first method which is called analogue mode, the signal are averaged for a large number of laser pulses inside of ICCD camera and the averaged data are transferred to a personal computer for analysis. The size of the scattered signal and the size of the background plasma emission signal can both be determined by this single measurement. This analogue method of data acquisition are adequate for initial Thomson scattering measurements, from capacity coupled discharges and dielectric barrier discharges with density above $10^{18}\,\mathrm{m}^{-3}$. However, for lower density discharges

photon counting method are used to acquire a high signal to noise ratio [23]. In photon counting methods, the detected signal level is compared to an externally set reference signal, and if the detected signal is larger than the reference signal, a single photon is considered to have been detected. In this method, the uncertainty in the detected signal is determined only by photon statistics. However, this method can only be used when the signal levels are expected to be extremely small, as signals which are due to multiple photons striking the photocathode are recorded as single photon events. This method is appropriate for the cases when the scattered signal and the background plasma emission is very small [6].

The detection system is calibrated using Rayleigh scattering from air or nitrogen gas at room temperature. The chamber is filled with air or nitrogen to pressure of several hundred torr, so that the Rayleigh scattered signal is much larger than the stray light signal. Both vacuum pump and gas inlet are closed to air not flow through the chamber. Measurement of the Rayleigh scattered signal using this procedure determine the response of the detection optics and ICCD camera.

2.4 Summary

In this chapter, the principle of laser scattering especially laser Thomson scattering were described. Then methods for calculation of electron density and electron temperature from measured data were described. The plasma sources used in this research were briefly mentioned. Finally, the experimental setup for non-thermal atmospheric pressure plasma were explained in details.

References

[1] A. scheeline, M.J. Zoellener, Thomson scattering as a diagnostic of atmospheric pressure discharges, Appl. Spectrosc. 38, 245 (1984).

[2] A.W. DeSilva, G.C. Goldenbaum, in: H.R. Griem, R.H. Lovberg (Eds.), Methods of Experimental Physics part A, 9, Academic Press, p. 61 (1970).

[3] J. Sheffield, Plasma Scattering of electromagnetic radiation, 2nd edition, Academic Press, (2011).

[4] Kelly Warner, Gary M. Hieftje, Thomson scattering from analytical plasmas, Spectrochimica Acta Part B, 57, 201 (2002).

[5] D. E. Evans, J. Katzenstein, Laser light scattering in laboratory plasmas, Rep. Prog. Phys. 32, 207 (1969).

[6] K. Muraoka, K. Uchino and M.D. Bowden, diagnostics of low-density glow discharge plasmas using Thomson scattering, Plasma Phys. Control. Fusion, 40, 1221 (1998).

[7] Sneep M and Ubachs W, Direct measurement of the Rayleigh scattering cross section in various gases J. Quant. Spectrosc. Radiat. Transfer, 92, 293 (2005).

[8] Sutton J A and Driscoll J F 2004 Rayleigh scattering cross sections of combustion species at 266, 355, and 532 nm for thermometry applications Opt. lett. Vol. 29, 2620 (2004).

[9] A F H van Gessel, E A D Carbone, P J Bruggeman and J J A M van der Mullen, Laser scattering on an atmospheric pressure plasma jet: disentangling Rayleigh, Raman and Thomson scattering, Plasma Source Sci. Technol. 21, 015003 (2012).

[10] W. Demotroder, Laser spectroscopy, Springer, (1995).

[11] D.E. Evans and J. Katzenstein. Laser light scattering in laboratory plasmas. Rep. Prog. Phys. 32, 207 (1969).

[12] H.J. Kunze. The laser as a tool for plasma diagnostics. In: Plasma Diagnostics (W.Lochte-Holtgreven, editor), North-Holland Publishing Company, Amsterdam p. 550 (1968).

[13] Marco van de Sande, Laser scattering on low temperature plasmas, Technische Universiteit Eindhoven, thesis, (2002).

[14] S. Hassaballa, K. Tomita, Y. K. Kim, K. Uchino, H. Hatanaka, Y. M. Kim, C. H. Park, K.

Muraoka: Jpn. J. Appl. Phys. 44, L442 (2005).

[15] S. Hassaballa, M. Yakushiji, Y. K. Kim, K. Tomita, K. Uchino, K. Muraoka: IEEE Trans. Plasma Sci. 32, 127 (2004).

[16] S. G. Belostotsiky, Rahul Khandelwal, Q. Wang, V. M. Donnelly, D. J. Economou, N. Sadeghi, Applied Physics Letters, 92, 221507 (2008).

[17] W. Siemens: Poggendorff's Ann. Phys. Chem. 102, 66 (1857).

[18] B. Eliasson, W. Egli, U. Kogelchatz: Pure Appl. Chem. 66, No. 6 1275 (1994).

[19] U. Kogelschatz: Plasma Chem. Plasma Processing **23**, No. 1, 1 (2003).

[20] A.Chirokov, A. Gutsol, and A. Fridman, Pure Appl. Chem., Vol. 77, No. 2, 487 (2005).

[21] T. Belmonte, G Arlnoult, G Henrion and T. Gries, J. Phys. D: Appl. Phys. 44, 363001

(2011).

[22] T Sakoda, S Momii, K Uchino, K Muraoka, N Bowden, M Maeda, Y Manabe, M Kitagawa,

and T Kimura, Japan, J. Appl. Phys. 30, L1425 (1991).

[23] A. Kono, K. Nakatani, Review of Scientific Instruments, Vol. 71, No. 7, 2716 (2000).

Chapter 3

Two-dimensional spatiotemporal measurements of electron density and electron temperature in non-thermal atmospheric pressure plasmas using laser Thomson scattering

Laser Thomson scattering (LTS) techniques has been applied to measure spatiotemporal evolution and two dimensional distribution of electron density (n_e) and electron temperature (T_e) in a capacity coupled micro-discharge (CCD) and dielectric barrier discharge (DBD) as two non-thermal plasma sources generated at around atmospheric pressure plasma. Such discharges are produced with good reproducibility by using a set of electrodes composed of a needle and a hemisphere with a spacing gap of 0.5 mm. First, the technique of applying LTS to micro discharge plasmas is presented. Then the spatiotemporal evolution measurement of electron density and electron temperature in two dimensions are presented and discussed.

3.1 Introduction

Non-thermal plasmas produced at atmospheric pressure have received attention as a result of their significant capacity for expanding application fields of plasmas such as plasma nano-science, plasma medicine, and plasma chemistry [1-5]. They have also key roles for applications such as the treatment of harmful exhausted gases, the ozone production, light sources, and recently, material processing. The dielectric barrier discharge (DBD) is one of the prominent methods to produce such plasmas [6-8]. For the applications of such plasmas, radicals generated in plasmas play key roles and their measurements are important for understanding chemical reactions in plasmas. Since generations of radicals are governed by free electrons in plasmas, measurements of electron density (n_e) and electron temperature (T_e) are prerequisite for diagnostics of plasmas. Therefore, in order to control and optimize these plasmas for the applications, understanding of discharge processes and plasma characteristics are needed. Non-thermal plasmas are usually composed of a lot of pulsed micro-discharges having a diameter less than 100 μm and their current durations are a few tens of nanoseconds for many cases [3, 6], so to know the characteristics of non-thermal atmospheric pressure plasmas, measurements of n_e and T_e of one pulsed discharge are needed. However, they are produced randomly both in time and in spatial position. Therefore, only limited diagnostics methods such as optical emission spectroscopy (OES) have been applied, and

complete understanding of these plasmas behavior have not yet been achieved. In order to contribute to the detail understanding of non-thermal atmospheric pressure plasmas, we have developed laser Thomson scattering (LTS) technique as a diagnostics method for the measurement of temporal evolution and spatial distribution of n_e and T_e in one pulsed micro-discharge. The LTS method can give local values of these plasma parameters with high spatial and temporal resolutions, if the method is appropriately utilized. This method have already been applied to high pressure plasmas such as micro-discharge plasmas for plasma display panels and laser-produced plasmas for extreme ultraviolet light sources, and have been shown advantages of LTS as a diagnostic method of them [9-13]. Especially for high pressure plasmas, the probing laser beams used for the LTS diagnostics may sometimes induce the perturbation in the plasmas. Therefore, the conditions under laser perturbation have been examined, and have been shown the way to avoid the laser perturbation in Ref. [14].

In order to apply LTS to pulsed discharge plasmas, they should be controlled well both in time and in position. Therefore, as a first target of the LTS diagnostics, we have selected a capacity coupled discharge (CCD) which is one of the types of non-thermal atmospheric plasmas. In CCD electrical circuit, there is a small capacitor in series with a pair of metal electrodes. For the case of CCD, there is no dielectric layer between the electrodes and the capacitor works as a dielectric layer of DBD that is the discharge can be truncated in a short time as the capacitor charges up. An external capacitor is connected in the series with the power supply circuit and the discharge electrode. After generation of the discharge, the charge accumulates in the external capacitor, then the voltage between the electrodes decreases, so the electrical discharge stops. In the CCD, electrode can be designed more freely, therefore, the controls of the position and the generation time of the pulsed micro-discharge is more easily compared to the other type of discharges such as the DBD. By selecting the shapes of metal electrodes appropriately, the position and the starting-time jitter of CCD can be easily adjusted. Besides, the discharge current of CCD can be easily controlled by changing the capacitor [15, 16]. Finally we produced a CCD plasma with excellent reproducibility. Next step, we extend the investigation to dielectric barrier micro discharge.

In this chapter, we present a LTS diagnostic system which have a good spatial resolution by using an ICCD camera as the detector. Also we show two-dimensional distributions of n_e and T_e in the CCD plasma with the spatial resolution of about 50 μm, while the diameter of the plasma are around 500 μm, and confirm the validity of the measured results. We also discuss about the results

of spatiotemporal evolutions of plasma parameters in the pulsed CCD as well as the diffusion, recombination process, and the energy balance of the discharge in recombination phase.

3.2 Experimental methods and procedure

The principle of LTS for the diagnostics of plasmas has been described in details in previous chapter. Therefore, we just here mention the principle to the extent necessary to understand the situation of LTS for this study. Thomson scattering is characterized by a parameter α as shown in following equation.

$$\alpha = \frac{1}{k\lambda_D} \qquad (1)$$

where k is the absolute value of the differential wave number vector determined by the incident laser wave number vector and the scattered light wave number vector, and λ_D is the Debye length. Since α is found to be in the range between 0.5 and 2 in this investigation, Thomson scattering is in collective regime. In the collective regime, the LTS spectrum consists of the ion term and the electron term. The ion term has a very narrow spectrum (< 0.1 nm) and is quite difficult to detect. On the other hand, the electron term is relatively broad (> 1 nm). Therefore, the electron term has been observed to diagnose the plasma in this study. As mentioned about α range, values of n_e and T_e can be evaluated by the spectral shape and the peak wavelength of the electron term [17, 18]. Besides, the absolute intensity of the electron term also gives information to determine the value of n_e, so this is used to check the consistency of the LTS.

3.2.1 Electrical circuit and electrode configuration

Figure 3.1 illustrates an electrical circuit for the generation of pulsed CCD. A capacitor C_1 (200 pF) is charged up to 3 kV by a DC power supply. By using a semiconductor switch (BEHLKE, HTS40-06), a pulsed voltage with a rapid rise time (10ns) is applied between electrodes. After an ignition of CCD, the external electric field between electrodes weakened because the discharge current charges up a capacitor C_2 (50 pF), which is connected with the discharge electrode in series, then the discharge stops. Afterwards, the charge accumulated by the C_2 attenuates by a time constant 50 µs by a resistance (1 MΩ) connected in parallel for the next generation of the pulsed CCD. Using this CCD circuit, it becomes possible to generate repeatedly the mono-polar pulsed CCD that disappears in a short time (less than 50 ns). The repetition rate of 10 HZ is set to synchronize the pulsed CCD plasma with the incident laser beam.

The electrical circuit for generation of dielectric barrier micro-discharge is similar as shown in Fig. 3.2. Bipolar high voltage is applied by two high voltage semiconductor switches. A Teflon layer with 200 μm thickness as a dielectric is coated on the surface of the hemispherical electrode.
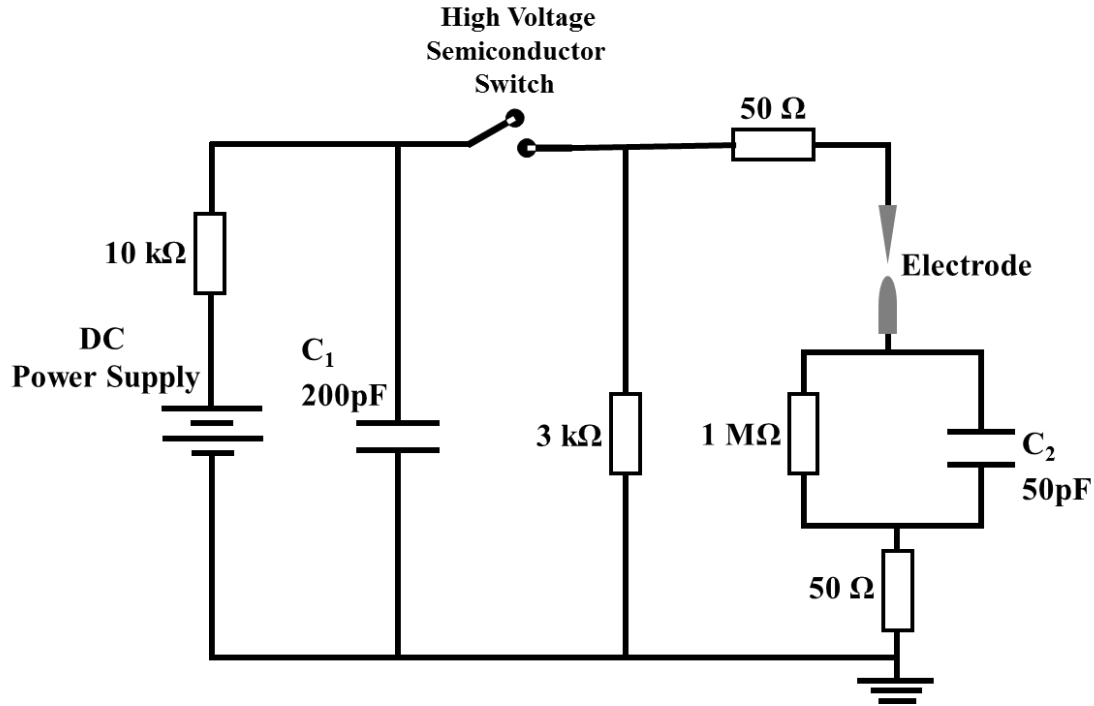

Fig. 3.1. The electrical circuit for pulsed CCD plasmas. A capacitor C_1 (200 pF) is charged by a DC power supply (Max. 5 kV), and a steep mono-polar pulse voltage is applied to the electrode with a semiconducting switch (BEHLKE, HTS50-06). After an ignition of CCD, a capacitor C_2 (50 pF) helps to vanish the plasma immediately.
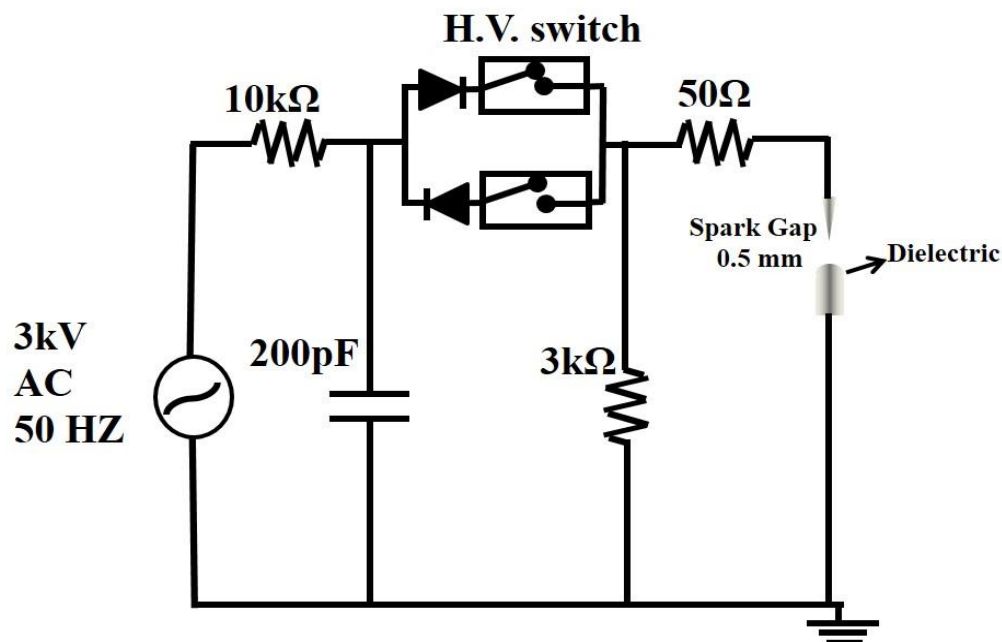
Fig. 3.2. The electrical circuit generates dielectric barrier micro discharges. A capacitor (200 pF) is charged by an AC power supply (3 kV) and a pulsed voltage is applied to the inter-electrode gap by two high voltage semiconductor switches.

Electrode configuration used in CCD experiment is shown in Fig. 3.3. The electrode set, which is consisted of needle electrode (φ=1.6 mm, a radius of curvature at the needle tip is 40 μm, because this condition achieve the minimum time jitter of the discharge) and a hemispherical electrode (φ=2.4 mm) with a separation gap of 0.5 mm, are placed in a vacuum chamber. These electrodes are made of tungsten. The mono-polar pulsed CCDs are generated in pure neon gas at a pressure of 400 Torr.

The generation position of the pulsed CCD was observed by optical emission images which are taken by the gated ICCD camera. A typical optical emission image of a pulsed CCD at t=5 ns is shown in Fig. 3.3. In this case, the gate width of the ICCD was set to be 2 ns. By comparing with several tens of the images, the difference of the position of the pulsed CCDs was estimated to be within ±30 μm. The timing jitter (within ±2 ns) is much shorter than the duration (around 40 ns) of the CCD and the electron decay state over 300 ns. And the position difference being within ±30 μm is smaller than the radius (about 1 mm) and the length (over 0.5 mm) of the CCD. Therefore, such temporal and spatial uncertainties of the generation of the pulsed CCD are regarded as not to affect the spatiotemporal measurements using LTS.

Waveforms of voltage and current of the discharge are shown in Fig. 3.4. The voltage of the hemispherical electrode can be calculated by dividing the electrical charge, which is the product of the electrical current and time, by the capacitance of the capacitor connected to the hemispherical electrode. Then, the voltage between electrodes (plotted in black) can be obtained by subtracting the voltage (voltage between the anode and the ground, plotted in red) applied to the needle electrode and the voltage to the hemispherical electrode. The rise-time of the discharge current is defined as $t = 0$ in this paper. The discharge current has a peak value of 13 A, and is vanished within 20 ns from the start. By integrating the current waveform, the total charge of the discharge was estimated to be 1.2×10^{-7} C. The time jitter of the discharge start was about ±2 ns. The difference of the position of each discharge was evaluated by taking many pictures of CCD plasmas using the ICCD camera. As a result, the difference was found to be within ±30 μm. Such temporal and spatial uncertainties were quite small compared to the discharge duration and the discharge size (~0.5 mm). Therefore, these uncertainties were found to be not a problem for the present study. This condition allows us to have reproducibility of the LTS signals at fixed time of the pulsed CCD.

3.2.2 Laser Thomson scattering applied to micro-discharge plasma

A schematic illustration of the LTS system used in this experiment has been shown in Fig. 3.5. The light source of LTS is the second harmonics beam (λ=532 nm) of the Nd:YAG laser (Continuum, Surelite III). The laser beam (pulse duration τ_L of 10 ns, repetition rate of 10 Hz) is focused and injected along with the x-axis between the electrode gap. In order to avoid a plasma perturbation and a breakdown by the laser injection itself, the laser energy (E_L) is chosen to be 5

mJ. The spot size (r_0) and the laser power density (W_L) at the focus point are about 50 μm and 2.6×10^{14} W/m^2, respectively. The LTS emission including Rayleigh scattering and stray light near 532 nm are focused on the entrance slit of a triple grating spectrometer (TGS) by a collecting lens perpendicular to the axes of the laser beam and the electrode set, and detected by a gated ICCD camera (Princeton, PI-MAX UNIGEN II, minimum gate width of 2 ns). Because the direction of the entrance slit height (10 mm) corresponds to the direction of the incident laser path, one-dimensional (x axis direction as shown in Fig. 3.3) spatially resolved measurements are achieved at the same time. The diameter of the discharge are around 500 μm at the middle of the discharge gap and the spatial resolution in the x direction are set to be 55 μm.
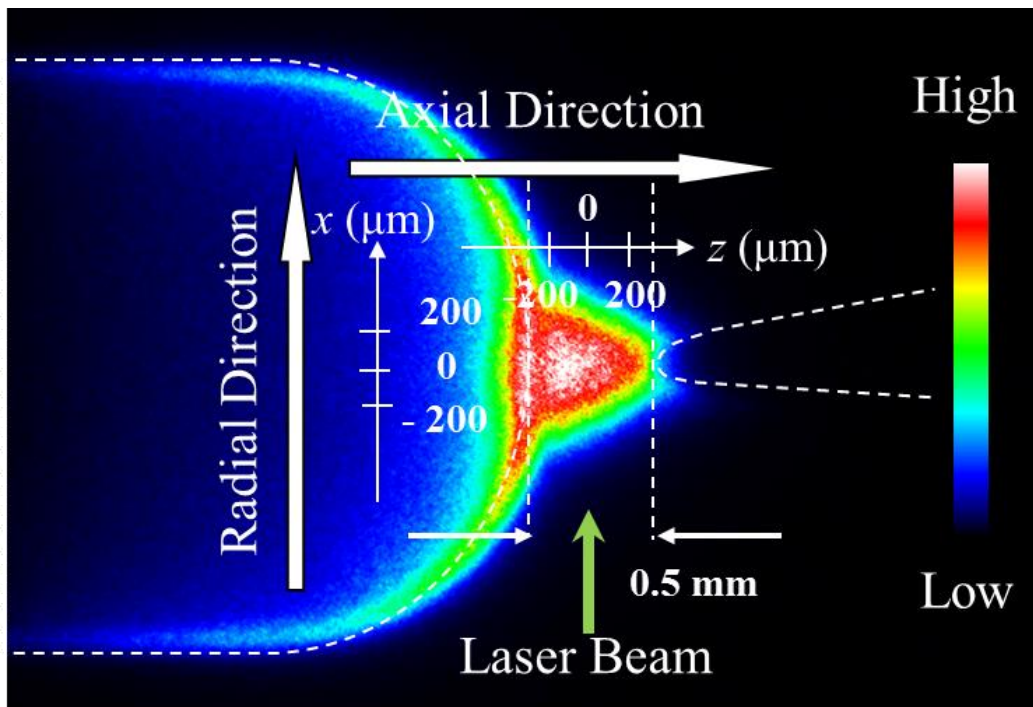

Fig. 3.3. A typical optical emission image of a filamentary pulsed CCD at t=5 ns measured with ICCD camera. It also shows electrode configuration of the CCD plasma. The electrode set is consisted with needle electrode (φ=1.6 mm, a radius of curvature at the needle tip is 40 μm) and a hemispherical electrode (φ=2.4 mm) with a separation gap of 0.5 mm. Radial direction (x) and Axial direction (z) are defined as described in this figure.
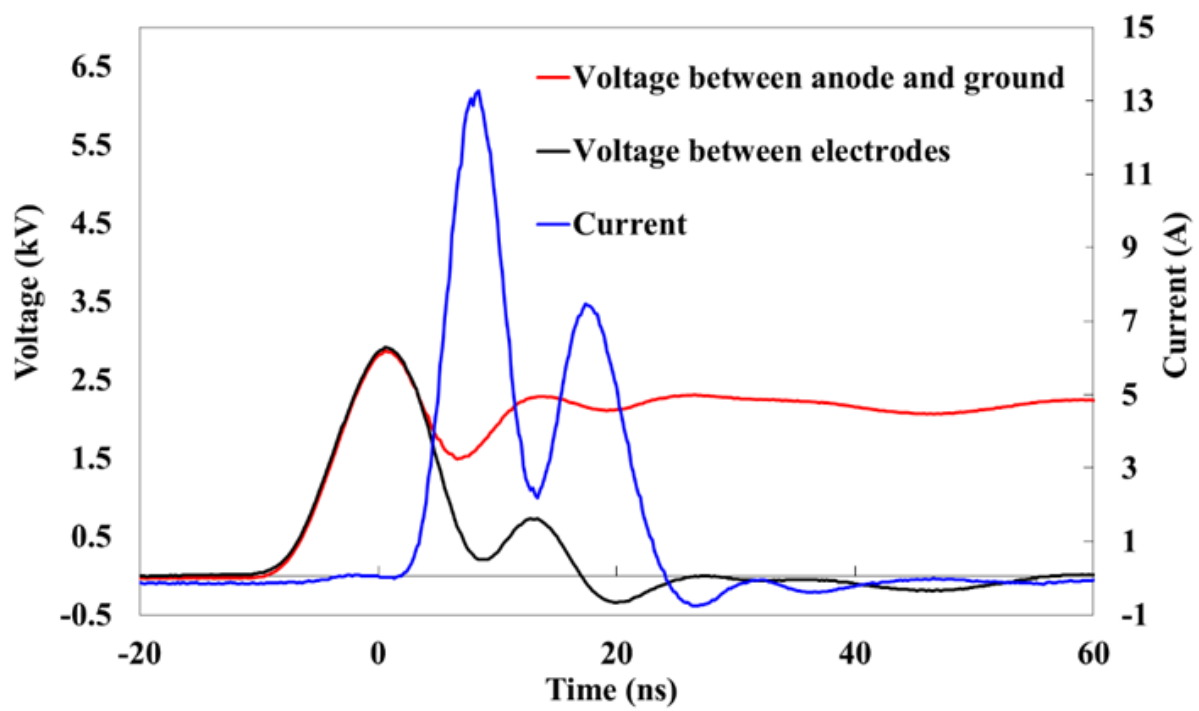
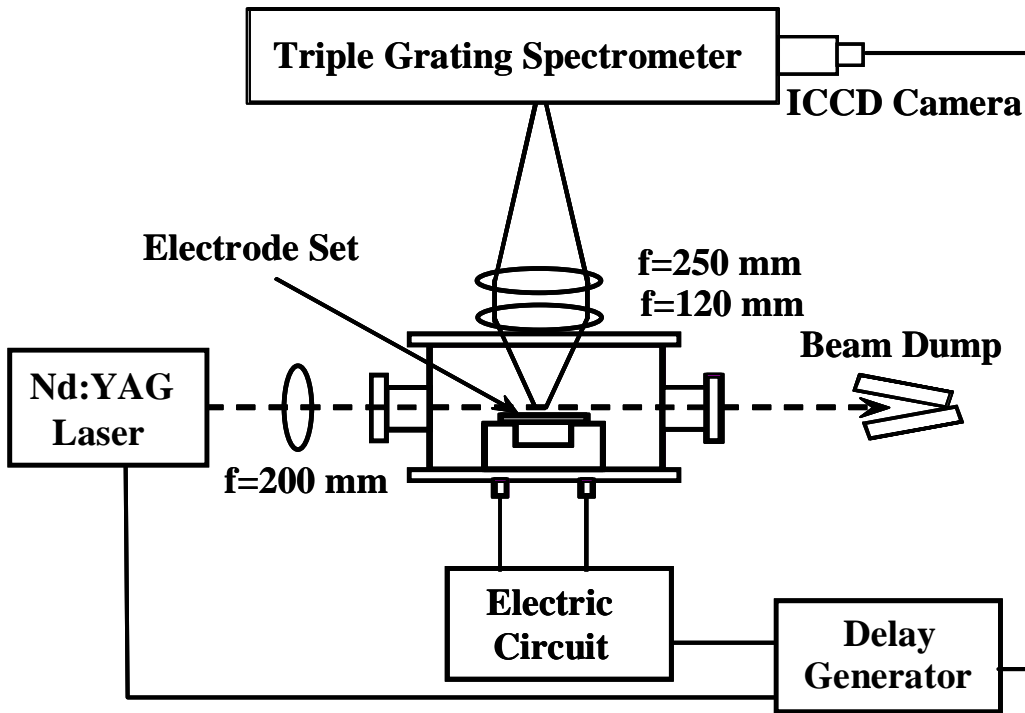Fig. 3.4. Voltage current characteristics of the CCD plasma

Fig. 3.5. Schematic illustration of the laser Thomson scattering system in micro discharge plasma

The configuration of TGS is shown in Fig. 3.6 and is almost the same as that used in other experiments [9-12, 19]. The LTS spectrum is broadened by kinetic motion of the electron in discharges, while spectral widths of the stray light and the Rayleigh scattering appearing at the incident laser wavelength are very narrow. A reverse-slit placed by the first focus position cuts only the laser wavelength part including the strong stray light and Rayleigh scattering from the incident light that is dispersed by the first grating. The only LTS spectrum is dispersed reversely by the following (second) grating, and is output from the second (normal) slit. In other words, the first part before the second slit plays the role to separate the LTS light from the incident light as same as an inverse dispersion double spectroscope. Finally, the LTS spectrum without the stray light and Rayleigh scattering, which is dispersed by the third grating, is detected by the ICCD camera. The rejection rate of the TGS was obtained to be 10^{-8} at a wavelength 1.0 nm away from

the laser wavelength. The spectral resolution of the light detecting system is achieved to be 0.34 nm at the case of the incident slit width of 100 μm.

In order to make spatial-resolved measurements under fixed alignments of the laser beam and the LTS detecting system, both electrodes were fixed on the *z*-axis translation stage, and moved by 10 μm with a micrometer. For the temporal-resolved measurements, the timings of the laser pulse and the gate of the ICCD, which are synchronized with a repetition rate of 10 Hz, are varied with respect to the pulsed CCD using two delay generators (SRS, DG-535). In order to increase the signal to noise ratio, the LTS spectrum was accumulated over 2000 times of the pulsed CCD by the gated ICCD camera and recorded by a computer based data acquisition system.
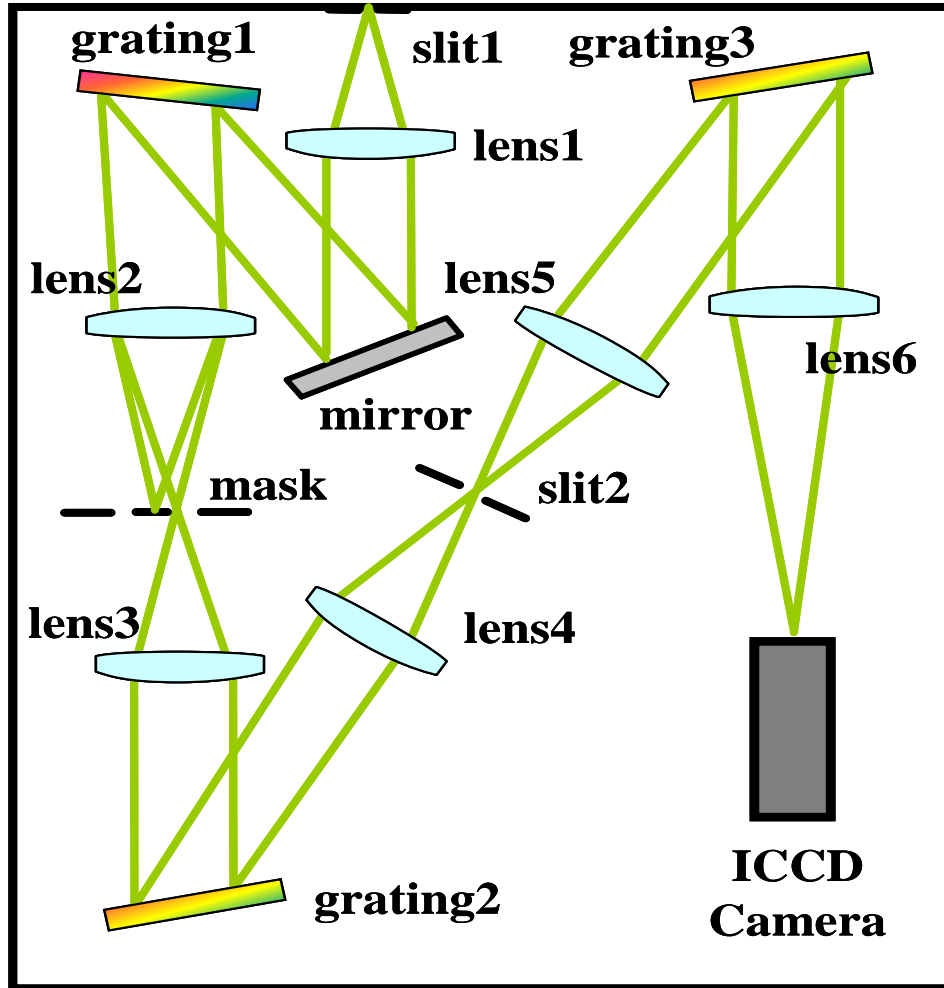

Fig. 3.6. Optical arrangement of the triple grating spectrometer with a mask for eliminating Rayleigh scattering and stray light.

3.3 Measurements of electron density and electron temperature using LTS

Figure 3.7 (a) and (d) show a LTS image measured from the pulsed CCD at t=15 ns and 205 ns, respectively. In both cases, the axial position z=0. The LTS intensity is represented by the color. Dark parts seen at the center of the LTS image are due to a wavelength stop near the laser wavelength ($\pm$0.8 nm) by the reverse-slit of the TGS. Because the x-axis is corresponding to the radial direction of the pulsed CCD, the radial profiles of n_e and T_e at one z position are derived from a LTS spectrum extracted from the LTS image. Figure 3.7 (b) and (c) shows a LTS spectrum at the z=0 and x=0 (center of the pulsed CCD) extracted from x=0 of Fig. 3.7 (a). Similarly, Fig. 3.7 (d) and (e) shows a LTS spectrum at the z=0 and x=0 extracted from x=0 of Fig. 3.7 (d). At almost times and places in the pulsed CCD, the LTS phenomena were in collective Thomson scattering regime. The n_e and the T_e can be evaluated from any two in shape, peak wavelength, and intensity of the LTS spectrum in the collective regime [20]. In this experiment, n_e and T_e were obtained in the fitting of the experimental data with the theoretical spectrum by the least squares method approximation. In order to demonstrate the relationships among n_e, T_e and LTS spectrum, Fig. 3.7 (b) and (e) show theoretical LTS spectra corresponding to different n_e and same T_e, and Fig. 3.7 (c) and (e) show theoretical LTS spectra corresponding to different T_e and same n_e. It can be seen from these figures that a 20% deviation of n_e or T_e gives clearly different spectrum. Because the solid curves are most close to the measured LTS spectra, we could conclude that $n_e = 4.5\times10^{22}$ m^{-3} and $T_e = 1.7$ eV for the spectrum measured at t=15 ns and $n_e = 1.8\times10^{22}$ m^{-3} and $T_e = 0.6$ eV for the spectrum measured at 205 ns. Over whole experiment from t=15 ns to 205 ns, the error ranges for these values were estimated to be within $\pm$20 %. It was also confirmed that the intensity of LTS, which was calibrated by the Rayleigh scattering from nitrogen gas, was consistent with the n_e and T_e deduced from the spectral shape and the peak wavelength.
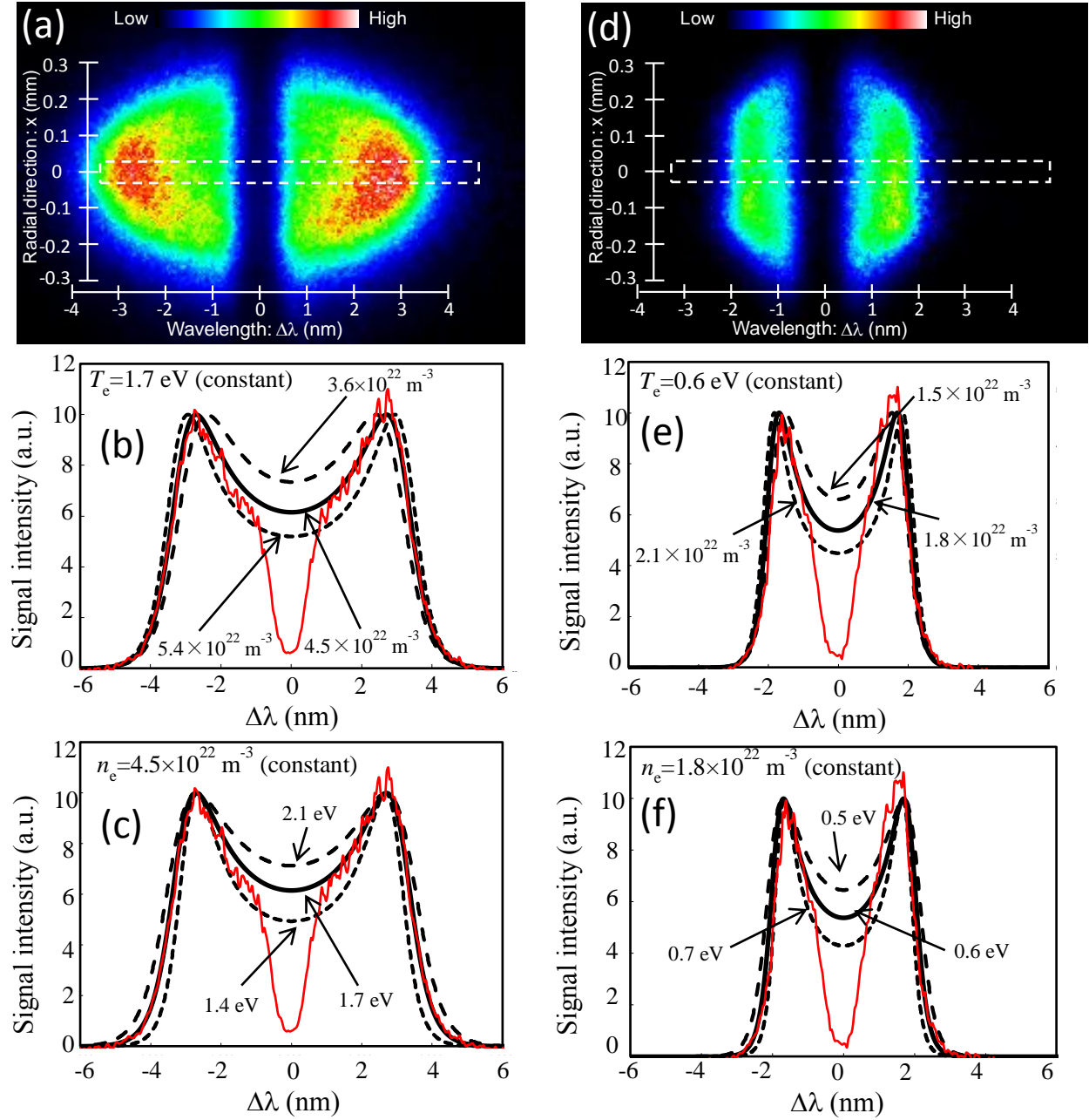
Fig. 3.7. Spectrum images of LTS signals measured in the CCD at t=15 ns (a) and 205 ns (d). In (b) and (c), the LTS spectrum at the z=0 and x=0 extracted from (a) are fitted by theoretical curves with slightly different parameters to check the sensitivity against the parameters. In (e) and (f), the LTS spectrum at the z=0 and x=0 extracted from (d) is also checked similarly.

Figures 3.8-3.11 show spatial distributions of n_e and T_e of the pulsed CCD at t=15 ns, 55 ns, 105 ns and 205 ns. For the measurements of spatial distributions of n_e and T_e, five axial positions were selected as shown in Fig. 3.3 (a). z=0 means the center of the electrode gap and z=100 μm and 200 μm are for the needle electrode side and z=-100 and -200 μm are for the hemispherical electrode side. Spatial resolution was 50×50×55 μm, which was determined mainly by the laser spot size. As clearly seen in Fig. 3.8 (a), at t=15 ns n_e are much different each place. At this time, the power input to the CCD is still large. n_e is peaked near the tip of the needle electrode (z=200 μm) where the electric field concentrates, and the value exceeds 10^{23} m^{-3}. On the other hand, even at the same time the n_e near the hemispherical electrode (z= -200 μm) is 10 times lower than that at z=200 μm, and the spatial distribution is flat over 500 μm. While the spatial distributions of T_e are z=100, 0, -100, -200 μm are flat and the values are around 1.5 (±0.5) eV. At t=55 ns (Fig. 3.9 (a) and (b)), the power input to the CCD is completely finished. The value of n_e starts to decrease and the T_e decreases about 0.9 eV. Finally at t=205 ns (Fig. 3.11 (a) and (b)), both of n_e and T_e take the same values in all places.

3.4 Estimation of gas temperature by rotational temperature measurement

In order to estimate the gas temperature (T_g) in the pulsed CCD, the rotational temperature of N_2 was obtained from the optical emission spectra of the 2nd positive system ($C^3\Pi_u \rightarrow B^3\Pi_g$, λ=375 − 381 nm) [21]. In this experiment, a pulsed CCD was generated in a mixture gas of 0.1 % of N_2 and pure Ne at 400 Torr. The optical detection system was almost the same as that of the LTS measurements. The only exception was to remove the reverse-slit from the TGS. The entrance slit width of the TGS was set at 50 μm, and the gate width of the ICCD camera was set at 10 ns. In order to perform the measurement with a good signal to noise ratio, optical emission of the N_2 2nd positive system was accumulated for 20000 times of the pulsed CCD. The T_g was estimated from the obtained emission spectrum of the N_2 2nd positive system, as assuming the gas temperature is equal with the rotational temperature. As a result, no apparent increase of T_g from room temperature was observed. The T_g in the pulsed CCD was found to be below 400 K because the accuracy of the measurement was of ±100 K.
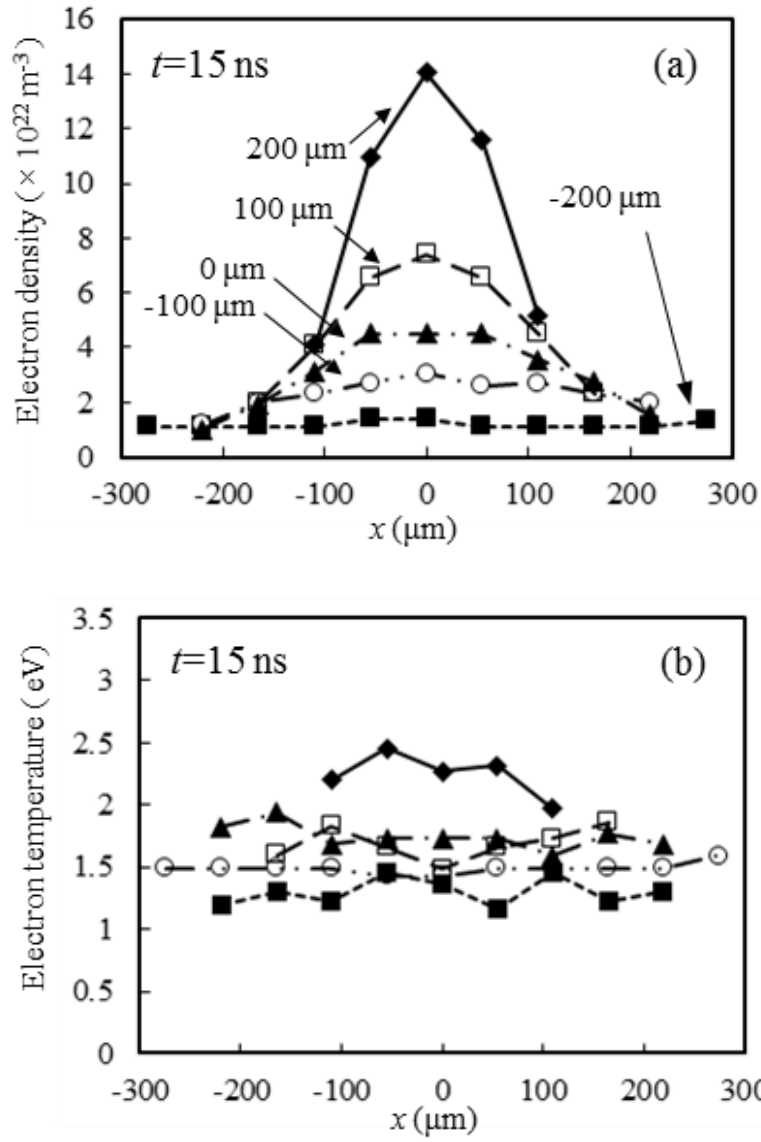
Fig. 3.8. Distributions of n_e (a) and T_e (b) in the pulsed CCD at t=15 ns.

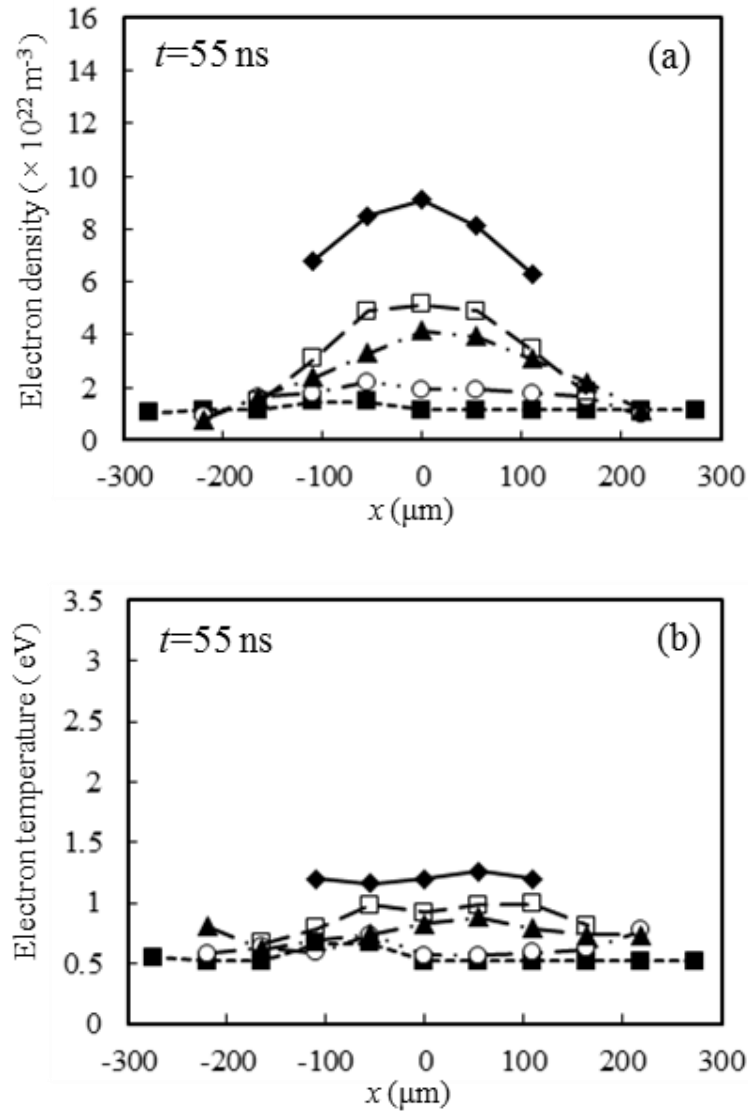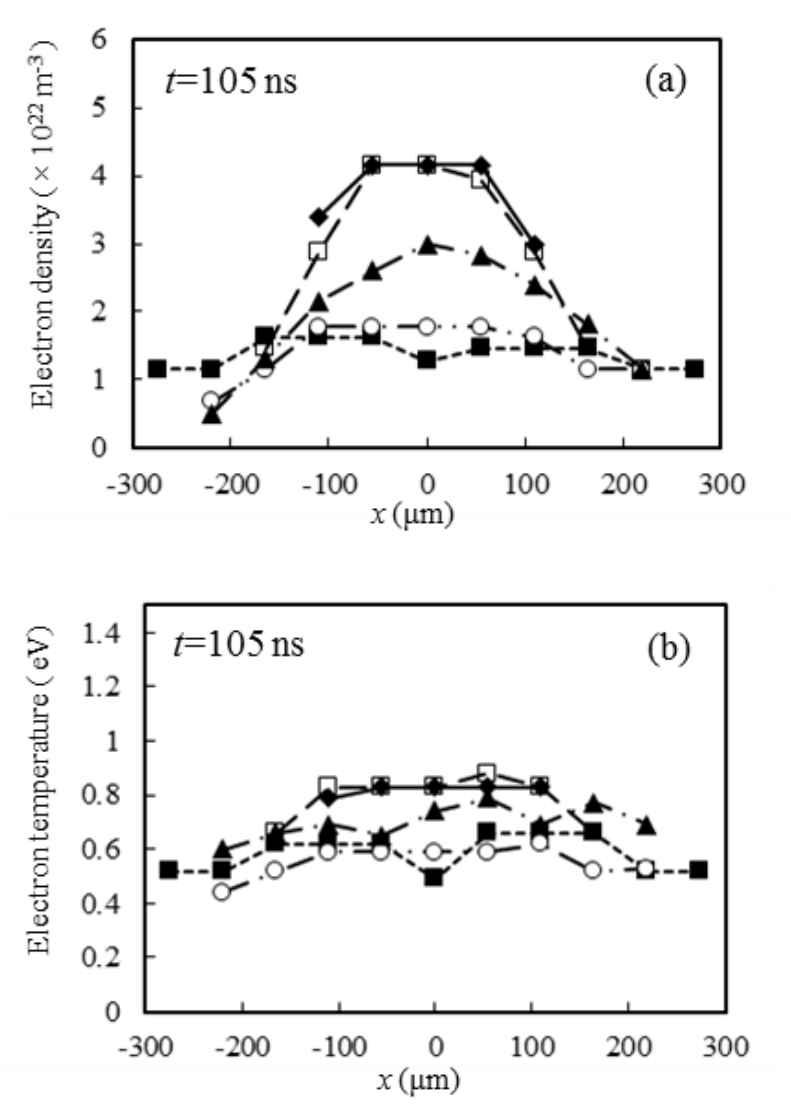Fig. 3.9. Distributions of n_e (a) and T_e (b) in the pulsed CCD at t=55 ns.

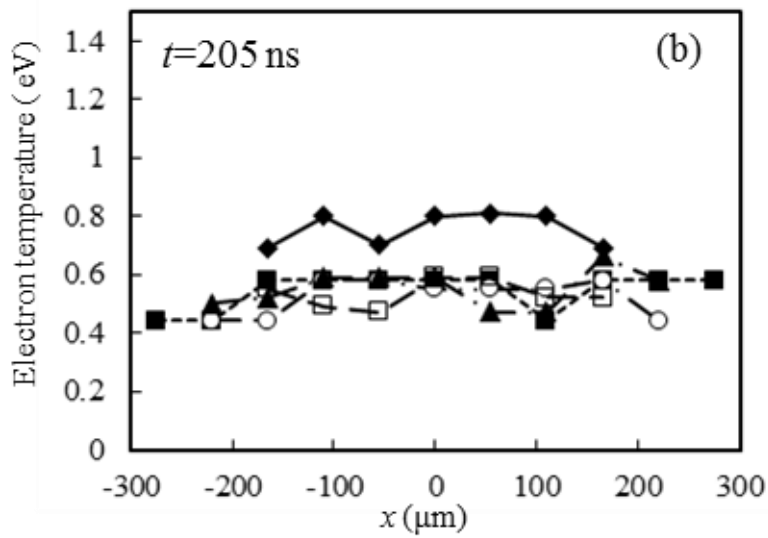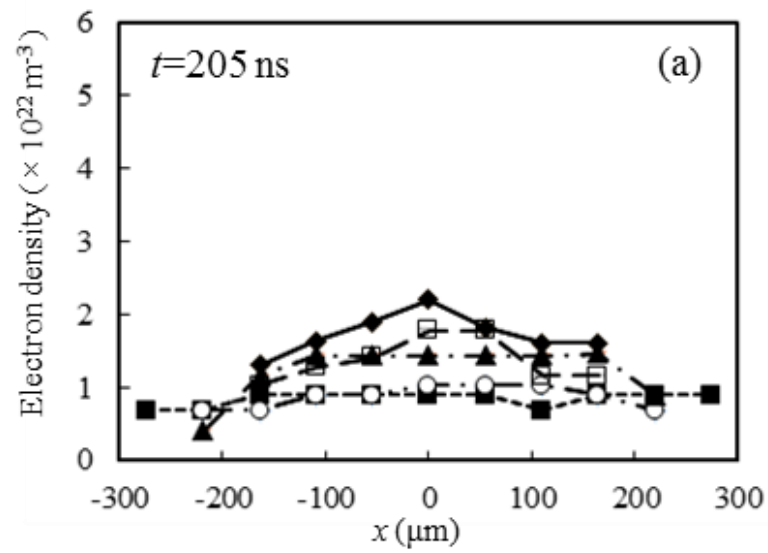Fig. 3.10. Distributions of n_e (a) and T_e (b) in the pulsed CCD at t=105 ns.

Fig. 3.11. Distributions of n_e (a) and T_e (b) in the pulsed CCD at t=205 ns.

3.5 Temporal variations of electron density and electron temperature

Fig. 3.12 shows temporal variations of n_e and T_e measured at the center of the discharge (z=0, x=0) by the LTS. The LTS measurements has been done at t=15, 25, 35, 55, 105, 205 ns. A big difference in the transient behavior between n_e and T_e has been observed. n_e remains almost constant with the value of 4.5×10^{22} m^{-3} for the first 40 ns, and afterwards decreases monotonously to 1.7×10^{22} m^{-3} at 205 ns with a time constant. The decreases of n_e after t=15 ns is considered to be dominated mainly by diffusion and recombination because the input of the electric power to the discharge is almost stopped after that time. A diffusion of electrons in plasma is expressed by a following eq. (2);

$$\frac{dn_e}{dt} = -D_a \nabla^2 n_e \tag{2}$$

where D_a is the ambipolar diffusion constant and approximated by eq. (3);

$$D_a \approx \mu_i \frac{\kappa_B T_e}{e} \tag{3}$$

where μ_i ($=e/m_i\nu_{in}$) is a mobility of ion, κ_B is the Boltzmann constant, m_i is mass of ion (Ne$^+$) and ν_{in} is collision frequency between ion and neutral. Using these equations, the D_a in the present CCD was estimated to be 1.8×10^{-3} m^2/s by using T_g=300 K and T_e=0.8 eV. Therefore, the radius extension width (Δr; $\Delta r = (D_a t)^{1/2}$) of the CCD from t=15 ns to 205 ns by the diffusion is estimated to be less than 20 μm. Because the diameter of the CCD was more than 600 μm, a contribution of the diffusion to the decrease of n_e at the center of the CCD was estimated about 10%. Based on the spatial profile in Fig.3.9 and Fig. 3.11 at time duration between 55 ns and 205 ns, the radial flux and the rate of decreasing electrons in surrounded area of 4×10^{-7} m^2 are calculated to be 8×10^{16} s^{-1} and 6×10^{18}s^{-1}, respectively. By this consideration, it is concluded that the diffusion is not main factor of the decrease of n_e. Next, the decrease of n_e by means of recombination is discussed.

3.5.1 Recombination mechanism in neon plasma at around atmospheric pressure

Electron-ion recombination is highly exothermic process. The process should therefore have a specific channel of accumulation energy consumption related to either dissociation of molecules, three-body collisions, or radiation, defining the three major groups of mechanisms of electron-ion recombination as follows:

Dissociative electron-ion recombination: The fastest electron neutralization mechanism in molecular gases or, in the presence of molecular ions, is dissociative electron-ion recombination:

$$e + AB^+ \longrightarrow (AB)^* \longrightarrow A + B^*$$

Recombination energy in these processes goes into dissociation of the intermediately formed molecule ion and to excitation of the dissociation products. These processes are common for molecular gases, but they can also be important in atomic gases because of the formation of molecular ions in the ion conversion processes:

$$A^+ + A + A \longrightarrow A_2^+ + A$$
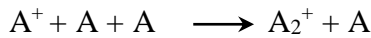
The dissociative recombination mechanism is quite fast and plays the major role in molecular gases. Reaction rate coefficients for most of the diatomic and three-atomic ions are in the order of 10^{-13} m^3s^1. The process has no activation energy, so its dependencies on both electron T_e and gas T_0 temperatures are not strong:

$$K_r^{ei}(T_e,T_0) \: \alpha \: 1/T_0T_e^{0.5} \qquad (4)$$

If the pressure is high enough, the recombination of atomic ions such as Ne^+ proceeds through the preliminary formation of molecular ions as described by equation 2. The molecular ion can then be fast neutralized in the rapid process of dissociative recombination. The ion conversion reaction rate coefficients are quite high.

When the pressure exceeds of 10 torr the ion conversion is usually faster than the following process of dissociative recombination, which becomes a limiting stage in the overall recombination kinetics.

Three-body electron-ion recombination: The electron-ion neutralization can be provided by a three-body electron – ion recombination in atomic gases in the absence of molecular ions:

$$e + e + A^+ \longrightarrow A^* + e$$
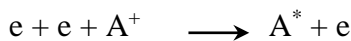
Energy excess in this case goes into kinetic energy of a free electron, which participate in the recombination act as a third body partner. Note that heavy particles (ions and neutrals) are unable to accumulate electron recombination energy fast enough in their kinetic energy, and are

ineffective as the third body partner. The three body recombination process described by equation 3 is the most important one in high-density quasi-equilibrium plasmas. Concentrations of molecular ions are very low in this case (because of the thermal dissociation) for the fast mechanism of dissociative recombination, and the three body reaction dominates. The three-body electron-ion recombination process described by equation 3 is reverse process with respect to the stepwise ionization. For this reason, the rate coefficient of the recombination can be derived from stepwise ionization rate coefficient and the Saha thermodynamic equation. For practical calculations, recombination rate coefficient can be presented in the numerical form:

$$K_r^{eei} = (\sigma_0/I)10^{-8}(I/T_e)^{4.5} \qquad (5)$$

Where K_r^{eei} is measured in m^6s^{-1}, σ_0 (m^2) is the gas-kinetic cross section and I and T_e are the ionization potential and electron temperature (eV). Typical values of K_r^{eei} at room temperature are about 10^{-32} m^6s^{-1}; at T_e=1 eV, this rate coefficient is about 10^{-39} m^6s^{-1}. At room temperature, the three-body recombination is able to compete with the dissociative recombination when the electron concentration is quite high and exceeds 10^{19} m^{-3}.

The equation representing the decrease of n_e by recombination is shown as follow [22, 23]:

$$\frac{dn_e}{dt} = -\alpha n_e^2 \qquad eq. (6)$$

Where α is recombination coefficient of electrons. As mentioned before, there are several mechanisms for electron-ion recombination. In a plasma with high electron density and relatively low temperature (1-2 eV), the three body recombination process is much faster than by a simple two-body radiative process. In such plasma, electrons recombine with positive ions by a three body process. In atmospheric pressure plasma, whether molecular or monoatomic gas, a two-step reaction for recombination of electrons in plasma has been proposed [24-26].

First step is formation of molecular ions. A three-body collision forms Ne_2^+ molecular ion.

$$Ne^+ + 2Ne \longrightarrow Ne_2^+ + Ne$$
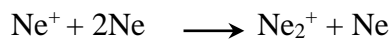
Second step is dissociative recombination of the molecular ions

$$Ne_2^+ + e \longrightarrow Ne + Ne^*$$
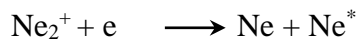
If the pressure is high enough (above 200 torr), the conversion of atomic ions proceed through the first step to form molecular ions. The ion conversion reaction rate coefficients are quite high. Also in this two-step process, decay time speed is determined by the first step. Because the process speed of the second step in experimental situation is much high and the molecular ion can be fast neutralized in the rapid process of dissociative recombination. The dissociative recombination rate coefficient is not so strongly dependent on the electron temperature. This rate is a dependency of $T_e^{-0.43}$.

The three body electron-ion recombination reaction is as following:

$$Ne^+ + 2e \longrightarrow Ne^* + e$$
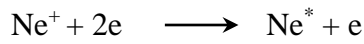
The three-particle electron-ion recombination plays key role in high density quasi-equilibrium plasma and it could be as a heating source for electrons. Energy excess goes into the kinetic energy of a free electron which participates as a third body partner in this recombination. The rate coefficient has a dependency of $\alpha \propto T_e^{-9/2}$ in this reaction [23-30]. Also the charge exchange reaction are taken into account.

$$Ne_2^+ + 2Ne \longrightarrow Ne^+ + 3Ne$$

According to above reactions, the electron density (n_e) can be calculated in recombination phase by eq. (6) as a function of time as well as ion (Ne^+) and dimer ion (Ne_2^+) density.

Recombination can be considered the dominant process for decreasing n_e because the power input to the discharge was truncated after $t = 20$ ns. In the present case, two recombination processes should be considered: three-body electron-ion recombination and neon-dimer ion (Ne_2^+) formation followed by dissociative recombination. Therefore, the following rate equations are utilized for the densities of the electron, neon ion (Ne^+), and Ne_2^+:

$$n_e = [Ne^+] + [Ne_2^+] \qquad (7)$$

$$\frac{d[Ne^+]}{dt} = -k_1 n_e{}^2 [Ne^+] - k_2 [Ne^+][Ne]^2 \qquad (8)$$

$$\frac{d[Ne_2^+]}{dt} = k_2 [Ne^+][Ne]^2 - k_3 n_e [Ne_2^+] \qquad (9)$$

Here, $[Ne]$, $[Ne^+]$, and $[Ne_2^+]$ are the densities of the neon atom, Ne^+, and Ne_2^+, respectively. We assume $[Ne]$ to be constant at a value of 1.3×10^{25} m^{-3}, while k_1, k_2, and k_3 are the rate coefficients of the three-body electron-ion recombination (m^{6}s^{-1}), dimer-ion formation (m^{6}s^{-1}), and dissociative recombination (m^{3}s^{-1}), respectively. The related reactions, values of the three coefficients, and source references are shown in table 1.

In Fig. 3.12, three curves calculated from the rate equations are shown, which are normalized to the experimental n_e data point at t = 25 ns when the ionization process becomes unimportant. The dot-dashed curve is calculated using two recombination processes. The dashed curve is calculated based on the formation process of the molecular ions and dissociative recombination ($k_1 = 0$, in this case). The dotted curve is calculated by assuming that the three-body electron-ion recombination is the only process ($k_2 = k_3 = 0$). Obviously, the calculated density decay of the dot-dashed line at t = 205 ns is approximately half the experimental value.

Note that the rate coefficients have some ambiguity. Since the 1960s, the rate coefficients of the three-body electron-ion recombination have been analyzed based on experiments and the collisional-radiative model [31, 32] with the assumption that the coefficients are the same for all noble gases [22, 23]. However, some reported values differ by a factor of 3 or more [27, 29, 33, and 34]. The k_1 value used here was reported to have an ambiguity of a factor 3 in Ref. 29. The three-body electron-ion recombination process is important for the electron density region larger than 10^{22} m^{-3}. Moreover, the three-body recombination process can be a possible heating source for electrons in the density decay phase as we will discuss in more detail later [28, 31]. The

coefficient k_3 has also been reported to have an ambiguity of a factor 10 [24]. However, the rate of the dimer-ion dissociative recombination is much larger than the rate of the dimer-ion formation. Thus, in this case, the ambiguity of k_3 does not significantly affect the current result. The value of the rate coefficient k_2 used here [35] has been adopted for excimer laser [36] and plasma display panel [26] studies. Finally, note that the electron density in this study is larger than those of the discharge plasmas of such applications by one or two orders of magnitude. For the present case, it may be necessary to consider the process that breaks the dimer-ions into Ne ions and Ne atoms.
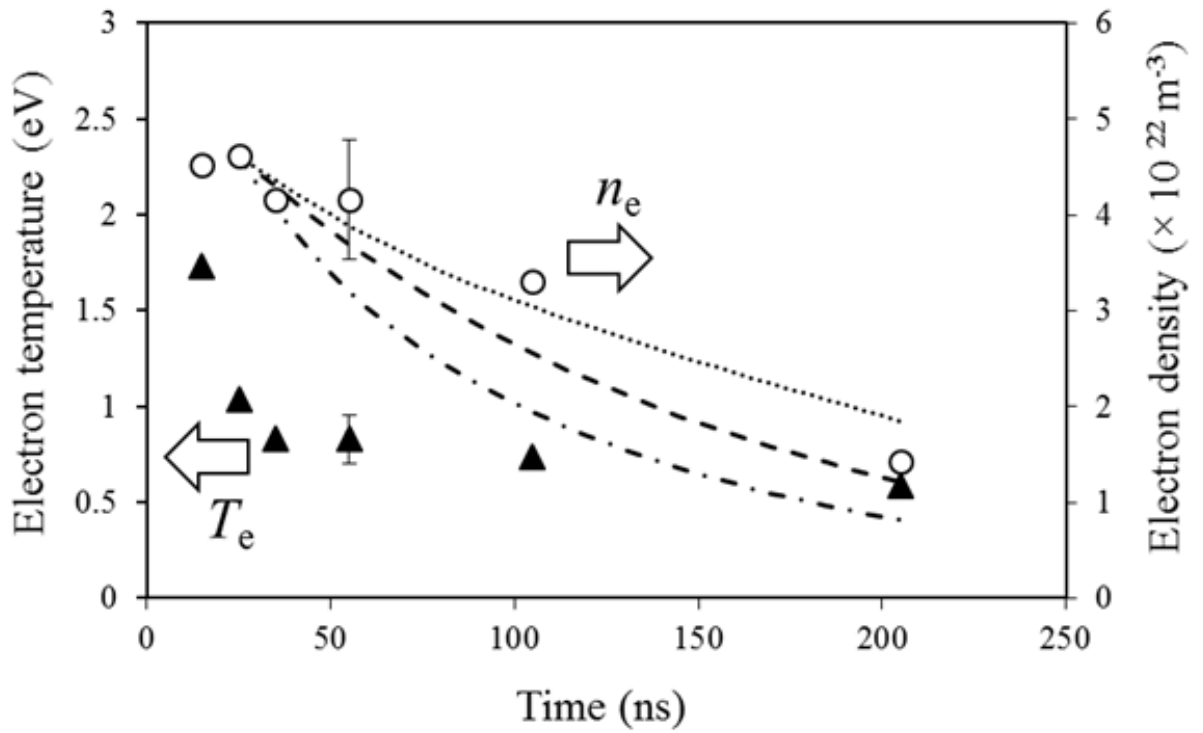

Fig. 3.12 Temporal variations of n_e and T_e measured at the discharge center at $z = 0$ and $x = 0$. The dotted line shows the calculated electron density by three-body electron-ion recombination, the dashed line indicates the calculated electron density by dissociative recombination, and the dot-dashed line represents the calculated electron density by both recombination processes.

Table 1. Reactions and rate coefficients.

Reactions	Rate coefficients	Ref.
Three-body recombination $Ne^+ + 2e \longrightarrow Ne + e$	$k_1 = 1.7 \times 10^{-39} T_e^{-4.5}$ $(m^6 s^{-1})$	29
Dimer ion formation $Ne^+ + 2Ne \longrightarrow Ne_2^+ + Ne$	$k_2 = 4.4 \times 10^{-44}$ $(m^6 s^{-1})$	35
Dissociative recombination $Ne_2^+ + e \longrightarrow Ne^* + Ne$	$k_3 = 3.7 \times 10^{-14} T_e^{-0.43}$ $(m^3 s^{-1})$	35

T_e in eV.

3.6 Electron particle collision and energy balances

As shown in Fig. 3.12, T_e is 1.7 eV at $t = 15$ ns during electrical power input; however, this rapidly decreases to 0.8 eV at $t = 35$ ns. After that time, T_e behaves a gradual decrease, and the decrease is a little about 0.2 eV for 170 ns from $t=35$ ns to 205 ns. The rapid decrease of T_e can be explained with two processes: the termination of the power input to the discharge at $t = 20$ ns, and the energy transfer between the electron and neutral particles or ions by elastic collision. The main reason of a rapid decrease of T_e observed to $t=35$ ns is considered to be the energy transfer by elastic collision between the electron and the neutral particle and/or the ion. Therefore, we consider the collision frequency of electrons with neutral particles (v_{en}) and with ions (v_{ei}).

The collision frequency of electron with neutral particle (v_{en}) and the one with ion (v_{ei}) are shown respectively by the following equations:

$$v_{en} = \frac{< v_e >}{\lambda_{en}} = \sqrt{\frac{8\kappa_B T_e}{\pi m_e}} n_0 \sigma_{Ne} \ , \quad v_{ei} = 2.9 \times 10^{-12} n_e \ln \Lambda / T_e^{3/2} \tag{10}$$

where $<v_e>$ is root-mean-square velocity of electron, λ_{en} is mean free path of electron to neutral particle, m_e is mass of electron, n_0 is density of neutral particle, σ_{Ne} ($= 5.2 \times 10^{-20}$ m^2) is collisional cross section of neon and $\ln \Lambda \approx 10$ is the Coulomb logarithm. Assuming the averaged of T_e and n_e to be 1.5 eV and 4×10^{22} m^{-3}, respectively, at the central part of the discharge, the total collision frequency v_e ($= v_{en} + v_{ei}$) is estimated to be about 1×10^{12} Hz. This value shows little change from $t = 15$ ns to 205 ns.

Thermal relaxation time (τ_r) of electrons with the neutral particles is defined as a following equation;

$$\tau_r \approx \left(1 - \frac{T_g}{T_e}\right)\left(\frac{m_g}{2m_e}\right) \Big/ v_e \tag{11}$$

Where T_g is gas temperature and m_g is mass of the neutral (neon). The thermal relaxation time of electrons with neutral particles (Ne atoms) is calculated to be less than 20 ns with the assumption that T_e and T_g to be 1.5 eV and 300 K, respectively. By considering this time, it is understood that the energy of the electron is able to be transferred to the neutral particle in a short time as a compare with large value of total collision frequency.

As mentioned before, T_e behaves a gradual decrease from t=35 ns to 205 ns and the decrease is a little about 0.2 eV for 170 ns. In order to explain this behavior, energy balance of a free electron after t=35 ns is discussed. It is considered that the energy dissipation of free electron occurs mainly through the elastic collision with the neutral particle and the ion. The power loss (P_{loss}) of the free electrons by the elastic collision can be estimated by eq. (12):

$$P_{loss} = 3T_e\nu_e(m_e/m_i)N \qquad (12)$$

Where N is total number of the free electron. Let's consider the power balance in the discharge region with a length of 100 μm at the center in the discharge axis. At $t = 205$ ns, the radius of the region is approximately 220 μm, the averaged electron density is 1.4×10^{22} m^{-3}, and the electron temperature is 0.6 eV. The power loss for electrons by elastic collisions with Ne atoms at room temperature in this region is estimated to be $P_{loss} \approx 2.3$ W (Calculated based on the spatial profile of electron density in Fig. 3.11 (a) at 200ns and $T_e = 0.6$ eV derived from Fig. 3.11 (b)). The electrical resistance in this volume is calculated to be 1.4 Ω, and the current necessary to support the electron temperature in the discharge volume by the ohmic heating power is approximately 1 A. However, no such current exist at t = 205 ns. On the other hand, the third free electron can receive energy through three-body electron-ion recombination. The third free electron can acquire the energy up to the total of the ionizing energy 21.6 eV of Ne and thermal energy 0.6 eV of the electron or less by the three body recombination. At this time, the recombination rate of electrons in this volume is estimated to be 2.2×10^{18} s^{-1}, and the power due to the release of Ne atom ionization energy (21.6 eV) into the discharge volume is estimated to be $P_{rec} \approx 7.6$ W. In this case, it is found that P_{rec} is about 3 times larger than P_{loss}. It is suggested that an energy transfer to the electron by three-body electron-ion recombination process suppresses a rapid decrease of T_e.

Here, the fact that P_{in} is 3 times larger than P_{out} is because of the uncomplicated assumption in which all the ionizing energy is transferred to the third free electron. However, of course, this assumption is not accurate. In the real case, considerable amount of ionizing energy should be given off through radiations. In order to know the accurate energy transferred to the third free electron, an investigation with the collisional-radiative model is needed. Concerning this problem, many studies have been done for expanding thermal plasmas (ETP) [29, 31]. In the study for ETP generated with Ar gas, it has been concluded that a part of ionizing energy (2.6 eV) goes to the third free electron by one three-body recombination event [29]. Since the ionizing energy of Ar is

15.75 eV, the energy of 2.6 eV corresponds to 17% of the total ionizing energy. Similarly, in the other study about ETP with several noble gases (Ne, Ar, and Xe) has shown that about 16% of ionizing energy should go to the third free electron by three-body recombination [37]. As shown in Fig. 3.12, around half of the free electron density decrease is a result of dimer-ion dissociative recombination. Based on these facts, the contribution of three-body recombination to the electron heating is estimated to be only 0.6 W. However, there are large ambiguities in the analysis of the recombination processes, and further study of this process is necessary.

3.7 Temporal variation of electron density and electron temperature in dielectric barrier micro-discharge

According to Fig. 3.13, the behavior of the electron density and the electron temperature are the same as CCD plasma. Electron density remains constant before 30ns. After that, it decreases gradually until 200ns. However, electron temperature decreases dramatically until 50ns after that it remains constant. To justify this trend, all the discussions in previous sections (3.5 and 3.6) can be extendable in DBD. Experimental study of plasma parameters behavior in nano-second pulsed filament in both dielectric barrier discharge and capacity coupled discharge can be comparable. First, we selected the capacity coupled discharge (CCD) instead of DBD to develop the diagnostic method of the pulsed filament discharge. The total electric charge that flows through the discharge channel vary from 20 nC to 850 nC by changing the capacitance in electrical circuit. We applied LTS successfully as a diagnostics method in pulsed filamentary discharge. Temporal evolution of electron density and electron temperature could also be measured as shown in Fig. 3.14 (a), (b). Finally, we could show that increase of total charge leads to increase of electron density; however, the electron temperature does not change.
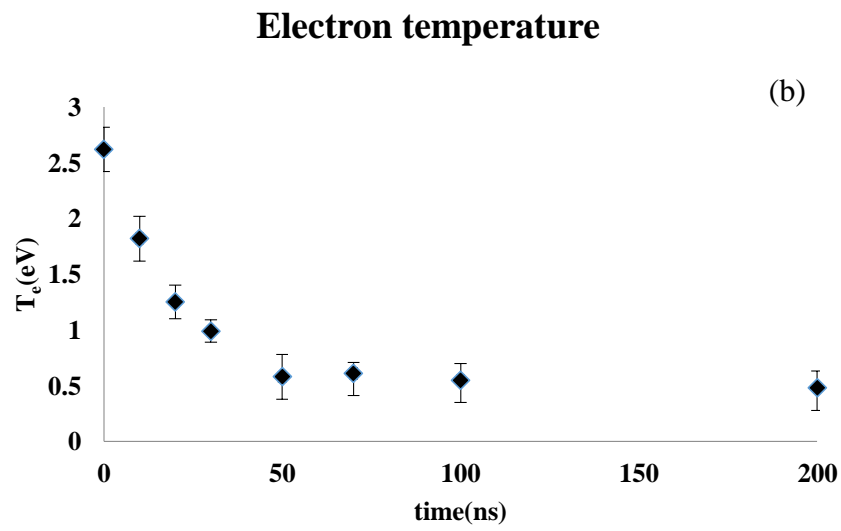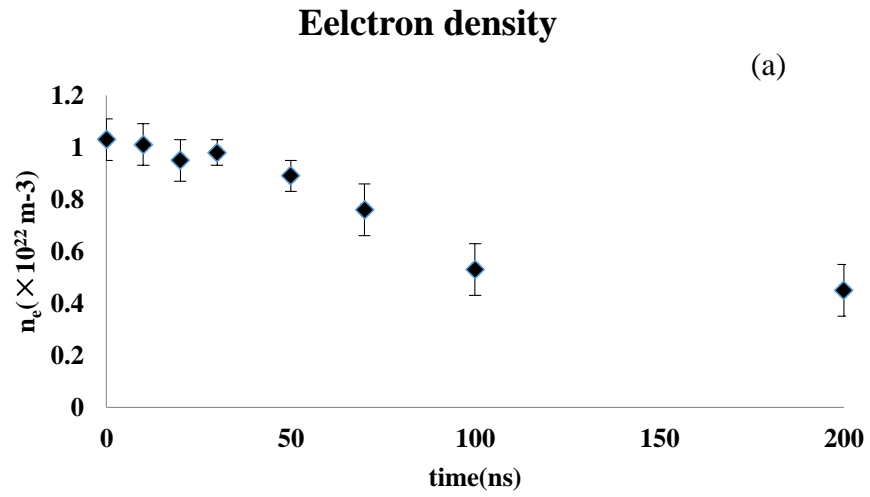
Eelctron density

(a)

Electron temperature

(b)

Fig. 3.13. Temporal evolution of electron density (a) and temporal evolution of electron temperature (b) in DBD.

Electron density
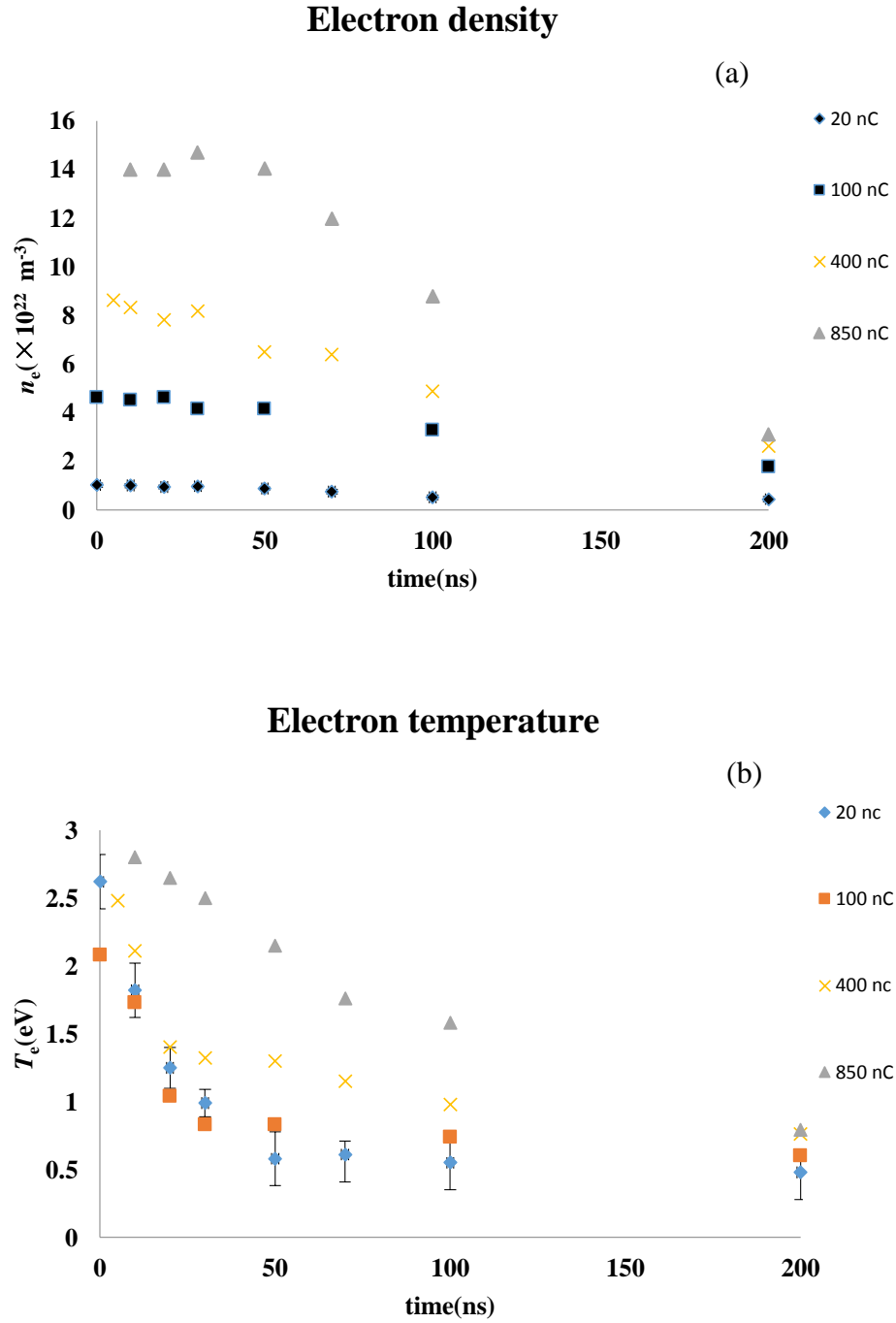
(a)

Electron temperature

(b)

Fig. 3.14. Temporal evolution of electron density (a) and electron temperature (b) with different total charge in pulsed filamentary discharge.

3.8 Laser perturbation in plasma

In this experimental condition, it is necessary to carefully consider T_e increasing (ΔT_e) due to inverse-bremsstrahlung process taken place by the laser incidence to plasmas. The thermal dose to the electron, which is well defined and formulated by Kunze *et al.* [38, 39] is reversely proportional to $T_e^{3/2}$ in proportion to the laser power density and n_e. In the filamentary pulsed CCD, it is considered that the laser heating becomes the maximum at $t=55$ ns when n_e ($=4\times10^{22}$ m^{-3}) is still high and T_e (~0.7 eV) has decreased rapidly, as can be seen in Fig. 3.12. Therefore, in order to observe the laser heating effect, the n_e and T_e at $t=55$ ns were measured using the LTS by changing the E_L as 1, 2.5, 5, and 10 mJ. As a result, n_e and T_e were the same values within the measurement error range of ±10 % at any E_L.

ΔT_e under the present condition ($n_e=4\times10^{22}$ m^{-3}, $T_e=0.7$ eV) is roughly estimated to be 0.6 eV at $E_L=10$ mJ ($W_L=5\times10^{14}$ W/m^2) by the equation of Kunze *et al.* In order to estimate the actual ΔT_e precisely, at least two effects have to be taking into account. When a thermal diffusivity ($\chi = \kappa/((5/2)n_e\kappa_B)$), κ: Spitzer's thermal conductivity) in plasma is large enough, the absorbed laser energy is distributed to the whole area expanded by Δr_L ($=(\chi\tau_L)^{1/2}$) to the radial direction in addition to laser spot (r_0) in the pulse duration (τ_L) of the laser [39]. Therefore, the estimated value of $\Delta T_e=0.6$ eV is overestimated for the portion of $(r_0/(r_0+\Delta r_L))^{1/2}$. Concerning this effect, ΔT_e in the laser spot is lowered to 0.1 eV, because of the $\chi=0.18$ m^2/s and $(r_0/(r_0+\Delta r_L))^{1/2}=0.14$ at $t=10$ ns in the present experimental condition. In addition, as considering that the thermal relaxation of electron with the neutral particle and the ion is 20 ns or less, 90 % or more of the absorbed laser energy is distributed to the neutral particle and the ion in r_0, as described in the previous section. As a result, the actual ΔT_e taking into account above two effects is estimated to be about 0.01 eV. It can be confirmed that there is no apparent difference on n_e and T_e measured at different laser energies. Therefore, it is concluded that the influence of an inverse-bremsstrahlung process by the laser incidence can be neglected in this experiment, and n_e and T_e of the filamentary pulsed CCD are precisely measured using the LTS.

3.9 Conclusion

Spatiotemporally-resolved measurements of the n_e and T_e of a pulsed CCD, which is one of the non-thermal plasmas generated at atmospheric pressure, have been performed using the LTS

technique. At the center of the discharge, n_e and T_e has been estimated to be 4.6 ($\pm$ 0.6)$\times 10^{22}$ m^{-3} and 1.7 ($\pm$ 0.3) eV, respectively, at the time of 15 ns after the start of the discharge. The obtained results are useful for discussing the particle balance and power balance of the discharge plasma. It has been found that the transient behavior of the pulsed CCD is dominated by the three-body electron-ion recombination because of high electron density as well as electron-ion dissociative recombination due to the formation of dimer ion in high pressure. Both of these mechanisms are operative in this system. It has also been found that the pulsed CCD is maintained in non-thermal state for a long time more than the thermal relaxation time that elastic collision became predominant. Finally, the results show that the LTS can be the powerful method to diagnose non-thermal atmospheric pressure plasmas.

LTS measurements have been successfully performed on the pulsed filament micro-discharge of DBD. Temporal evolution of electron density and temperature could also be measured. It has been investigated that the peak values of electron density and electron temperature at the center of the pulsed filament discharge are (1.03 $\pm$0.08)$\times 10^{22}$ m^{-3} and 2.62 ($\pm$0.2) eV, respectively. It has also been found that the behavior of the micro-discharge of DBD is governed by the three-body recombination and dissociative recombination.

For all cases (different total charges), the electron density decreases with a time constant of 100 ns. This decay time is consistent with three body recombination and dissociative recombination. Increasing of total charges leads to increasing electron density; however, electron temperature does not change significantly.

References

[1] W. Siemens: Poggendorff's Ann. Phys. Chem. 102, No. 66 (1857).

[2] B. Eliasson, W. Egli, U. Kogelchatz: Pure Appl. Chem. 66, 1275 (1994).

[3] U. Kogelschatz, B. Eliason, W. Egli: Pure Appl. Chem. 71, 1819 (1999).

[4] U. Kogelschatz: Plasma Chem. Plasma Processing 23, 1 (2003).

[5] T. Belmonte, G. Arlnoult, G. Henrion, T. Gries, J. Appl. Phys. D: Appl. Phys. 44, 363001 (2011).

[6] A.Chirokov, A. Gutsol, and A. Fridman, Pure Appl. Chem., Vol. 77, No. 2, 487 (2005).

[7] T. Belmonte, G Arlnoult, G Henrion and T. Gries, J. Phys. D: Appl. Phys. 44, 363001 (2011).

[8] S. Muller, R.-J. Zahn, Contrib. Plasma Phys, 47, No. 7, 520 (2007).

[9] S. Hassaballa, M. Yakushiji, Y. K. Kim, K. Tomita, K. Uchino, K. Muraoka: IEEE Trans. Plasma Sci. 32, 127 (2004).

[10] K. Tomita, T. Kagawa, K. Uchino, S. Katsuki, H. Akiyama: J. Plasma and Fusion Research 8, 488 (2009).

[11] S. Hassaballa, Y. Sonoda, K. Tomita, Y-K Kim, K Uchino: J. Soc. Information Display 13, 639 (2005).

[12] S. Hassaballa, K. Tomita, Y. K. Kim, K. Uchino, H. Hatanaka, Y. M. Kim, C. H. Park, K. Muraoka: Jpn. J. Appl. Phys. 44, L442 (2005).

[13] Y. Sonoda, S. Nishimoto, K. Tomita, S. Hassaballa, Y. Yamagata, K. Uchino: J. Plasma and Fusion Research, 8, 696 (2009).

[14] K. Tomita, S. Hassaballa, K. Uchino: IEEJ Trans. FM, 130 1099 (2010).

[15] H. Mase, T. Fujiwara, N. Sato: Appl. Phys. Lett. 83 5392 (2003).

[16] H. Mase, T. Fujiwara, N. Sato: IEEE Trans. Plasma Sci. **32** 380 (2004).

[17] D. H. Froula, S. H. Glenzer, N. C. Luhmann, Jr., J. Sheffield: Plasma Scattering of

Electromagnetic Radiation (Academic Press, USA, 2011) 2nd ed., chap. 5, p. 103.

[18] D.E. Evans, and J. Katzenstein: Rep. Prog. Phys. 32**,** 207 (1969).

[19] K. Tomita, N. Bolouki, H. Shirozono, Y. Yamagata, K. Uchino, K. Takaki, J.

Instrumentation, Vol. 7, C02057 (2012).

[20] D.H. Froula, S.H. Glenzer, N.C. Luhmann Jr., J. Sheffield, Plasma Scattering of
Electromagnetic Radiation (Academic press, 2011).

[21] S. Koike, T. Sakamoto, H. Kobori, H. Matsuura and H. Akatsuka: Jpn. J. Appl. Phys., 43,
5550 (2004).

[22] A. Funahashi, S. Takeda: J. Phys. Soc. Jpn, 25, 298 (1968).

[23] E. Hinnov, j. G. Hirschberg: Phys. Rev. 125, No. 3 795 (1962).

[24] S. V. Desai, Recombination of electrons and ions in an atmospheric argon plasma, J. Quant.

Spectrosc. Radiat. Transfer. Vol. 9,1371 (1969).

[25] J P Beouf, Plasma display panels: physics, recent developments and key issues, J. Phys. D:

Appl. Phys. 36, R53 (2003).

[26] J. Meunier, Ph. Belenguer, and J.P. Boeuf, Numerical model of an ac plasma display cell in

neonxenon mixtures, J. Appl. Phys. 78, 731 (1995).

[27] N. D'Angelo: Phys. Rev. 140, No. 5, A 1488 (1965).

[28] B. Makin, J. C. Keck: Phys. Rev. Lett. 11, No. 6, 281 (1963).

[29] M.C. M. van de Sanden, J. M. de Regt, D. C. Schram: Phys. Rev. E 47, No. 4 2792 (1993).

[30] A. Fridman, Plasma Chemistry (Cambridge University Press, 2008)

[31] D. R. Bates, A. E. Kingston, Nature, 189, 652 (1961).

[32] J. Vicek: J. Appl. Phys. 22, 623 (1989).

[33] P. Mansbach and J. Keck: Phys. Rev. 181, 275 (1969).

[34] M.R. Flannery: Adv. At. Mol. Opt. Phys. 32, 117 (1994).

[35] L.A. Levin, S.E. Moody, E.L. Klosterman, R.E. Center, J.J. Ewing: IEEE J. Quantum Electron. 17, No. 12, 2282 (1981).

[36] A. P. Vitols and H. J. Oskam: Phys. Rev. A. 5, No 6, 2618 (1972).

[37] S. E. Selezneva, M. I. Boulos, K. G. Letourneur, M. F. A. van Hest, M. C. M. van de Sanden, D. C. Schram: Plasma Sources Sci. Technol. 12, 107 (2003).

[38] W. L. Holtgreven, *Plasma Diagnostics* (North-Holland Publishing Company, Amsterdam, 1968).

[39] J. L. Walsh, F. Iza, M. G. Kong: Eur. Phys. J. D 60, (2010).

Chapter 4

Diagnostics of cathode-directed streamer using laser Thomson scattering

Laser Thomson scattering diagnostics has been developed for the study of the ionization waves in initial stages (streamer) of electrical discharge in pure helium gas. Temporal evolutions of electron density and electron temperature in streamer moving toward the cathode have been measured locally (2 mm near to needle) in helium electrical discharge. In order to avoid laser perturbation and obtain sufficient intensity of Thomson scattering signal, two cylindrical lenses have been used to optimize spot size of a probing laser at around focusing point. At position of 2 mm from the anode electrode (needle electrode), electron density (n_e) and electron temperature (T_e) have been measured to be around 10^{18} m^{-3} and 2 eV, respectively in the initial stage of the primary streamer.

4.1 Introduction

Atmospheric pressure plasmas produced by pulsed discharges are investigated as an effective source of non-equilibrium plasmas.   It is well known that the electrical breakdown at around atmospheric pressure is described by a streamer theory [1]. Based on the streamer dynamics, the initial stage of the electrical breakdown is the development of nonlinear ionization waves in a non-ionized medium, known as streamer discharges (or primary streamers), and finally it leads to the creation of a weakly ionized non-equilibrium plasma [2-4]. Then, the streamers cross the gap. This final stage of evolution is also known as a secondary streamer.

In the study of streamers, some have dealt with the structure and propagation of streamers. For instance, Ref. 5 measured the development of neon streamer as a function of the electric field strength and the streamer length. The propagation of air streamers and their dependence on the applied voltage, the distance between electrodes [6], and pressures [7] have been investigated. Time resolved measurements [8] have been successfully performed. Reference [9] measured and simulated pulsed streamer in three spatial dimensions. Furthermore, spectroscopic studies of streamer discharges have been reported. One of them is based on measurements and analyses of

absolute intensities of the second and first negative systems of molecular nitrogen to determine the reduced electric field and an electron number density [10, 11]. Also, Ono et al. applied optical diagnostics such as laser-induced florescence, laser absorption, and optical emission spectroscopy technique to measure density and temperature of different active species produced inside the pulsed streamer discharge under atmospheric pressure [12, 13]. However, there is no direct measurement on the primary streamer to examine temporal evolution of electron density n_e and electron temperature T_e.

Measurements of n_e and T_e are important to understand the basic structure of the streamer. Also, for the industrial applications of streamers, active species generated inside the streamers play key roles. Generation of such species is governed by free electrons inside the plasmas. Therefore, measurements of n_e and T_e are essential to understand the behavior of active species.

Laser Thomson scattering has been known as one of the most reliable method to measure n_e and T_e of plasmas. It also provides a high spatial resolution [14-19]. The successful application of LTS diagnostics to micro discharges (secondary streamers) has been reported [20]. However, there are two challenges when the LTS method is applied to the primary streamers. The first one is that, due to a small Thomson scattering cross-section and the low electron density in the primary streamer (on the order of 10^{18} m^{-3}), the scattering signal level becomes extremely low. The second one is the laser perturbation against the plasma electric state. Because the primary streamer accompanies the very high electric field, the superposition of the strong electromagnetic field in the laser spot may change the electric state in the streamer.

The current investigation aims to solve the above mentioned problems of the LTS method to diagnose the primary streamer and present temporal evolution of n_e and T_e in the initial stages of the cathode-directed streamer.

4.2 Experimental setup and procedure

The electrode set consists of a needle electrode (diameter of 1.6 mm) and a hemispherical electrode (diameter of 2.4 mm) with a gap distance of 16 mm. These electrodes are made of tungsten. The electrodes were placed in a vacuum chamber. The power was applied by repetitive nanosecond high-voltage pulses with a rise time of 10 ns and the peak voltage of 3 kV. The mono-polar high-voltage pulses were generated from a DC power supply using a fast high-

voltage semiconductor switch (BEHLKE HTS50-60) with repetition rate of 10 Hz. The mono-polar pulse generated pulsed discharge in pure helium gas at a pressure of 250 Torr. Our previous research report of the capacity coupled discharge [20] describes the similar experimental setup and electrical circuit. The polarity of applied voltage to the needle electrode was positive that it led to the formation of a positive streamer moving toward the cathode.

The principle of the Thomson scattering diagnostics has been already reviewed [19, 20], and therefore, we only mention that the Thomson scattering in this study is in the incoherent regime and the scattering is induced by electrons moving independently. The scattered light intensity gives the electron density n_e. The thermal motion of electrons makes the scattered spectrum to be Gaussian due to the Doppler broadening. So the spread of the scattered spectrum gives the electron temperature T_e.

The light source of the laser Thomson scattering was the second harmonic beam ($\lambda = 532$ nm) of a Nd:YAG laser (Continuum, Surelite III). The laser beam (pulse duration of 10 ns, repetition rate of 10 Hz) was focused by lens and injected inside the chamber between the electrodes gap. First, a plano-convex lens with focal length of 200 mm was employed to focus the laser beam with 8 mJ energy. This setting provided a spot size of 50 μm and a power density of 5×10^{14} W/m^2. This condition induced the perturbation of the electric state in the streamer. Then, it was replaced with a combination of two cylindrical lenses with focal lengths of 300 mm and 400 mm in order to avoid the laser perturbation. Further explanation on this issue will come at the next section. The Thomson scattering spectrum was analyzed by the triple-grating spectrometer (TGS). The configuration of the TGS, which was used to reduce the stray light, was almost the same as that used in other experiments [14-20]. Finally, the spectrum was detected by a gated ICCD camera (Princeton, PI-MAX UNIGEN II).

The propagation of pulsed streamer was observed by the gated ICCD camera directly and without the TGS. Figure 1 shows an optical emission image of streamer at different time. In this case, the gate width of the ICCD was set to be 2 ns and the accumulation number was 50.

In order to perform temporally-resolved measurements, the timing of the laser system and the ICCD camera, which were synchronized with the laser repetition rate of 10 Hz, were varied with respect to the pulsed discharge using two delay generators (SRS, DG-535). In order to increase

the signal to noise ratio, the LTS spectrum was accumulated over several thousand pulsed discharges by the ICCD camera and recorded by a computer based data acquisition system.

4.3 Results and Discussion

Based on the ICCD pictures shown in Fig. 4.1 and the waveforms of applied voltage and current shown in Fig. 4.2, two phases can be observed in the streamer: primary streamer and secondary streamer [12]. At the early stage, the primary steamer formed as a cloud in the duration of 0 to 70 ns. The streamer starts with an ionization cloud at the tip of the needle electrode (Fig. 4.1 (a), (b)). The time in Fig. 4.1 (a) is defined as a time origin (t = 0) in this paper. Then, the streamer expands as a spherical shell toward the hemispherical electrode at a distance of 16 mm as shown in Fig. 4.1 (c) and Fig.4.1 (d). After that, it reaches the hemispherical electrode (Fig. 4.1 (e)) and finally, by increasing the current, the secondary streamer is created (Fig. 4.1 (f)). The streamer velocity is calculated to be 10^5 m/s. This value is in good agreement with reported values [23].

The curvature radium of the tip of the needle electrode is around 40 μm, and therefore, the electric field intensity when the voltage of 3 kV is applied is estimated to be 8×10^7 V/m and the streamer discharge starts from this point. In order to observe the effect of the high electric field associated with the streamer, it is desirable to set the observation point as close to the needle tip as possible. However, at the point of 1 mm from the needle tip, for example, stray lights produced by the needle electrode obstructed the signal detection. Finally, the position at 2 mm from the needle tip was selected for the Thomson scattering measurement of this paper.

Figure 4.3 shows an example of the obtained LTS spectrum. Detailed conditions for this spectrum will be described later. In order to keep the signal to noise ratio of the measurement high enough, the photon-counting detection technique was employed. The Thomson scattering signals were accumulated by ICCD camera over 5000 laser shots. It can be seen from Fig. 4.3 that the measured spectrum is well fitted by a Gaussian curve. Therefore, we can determine values of n_e and T_e.

Since there is high electric field in the primary streamer particularly near the needle electrode, frequent electron-impact excitations of the gas atoms may take place in this region. Hence, there

is a probability of the laser perturbation by the strong electromagnetic field by the probing laser with a high power density.
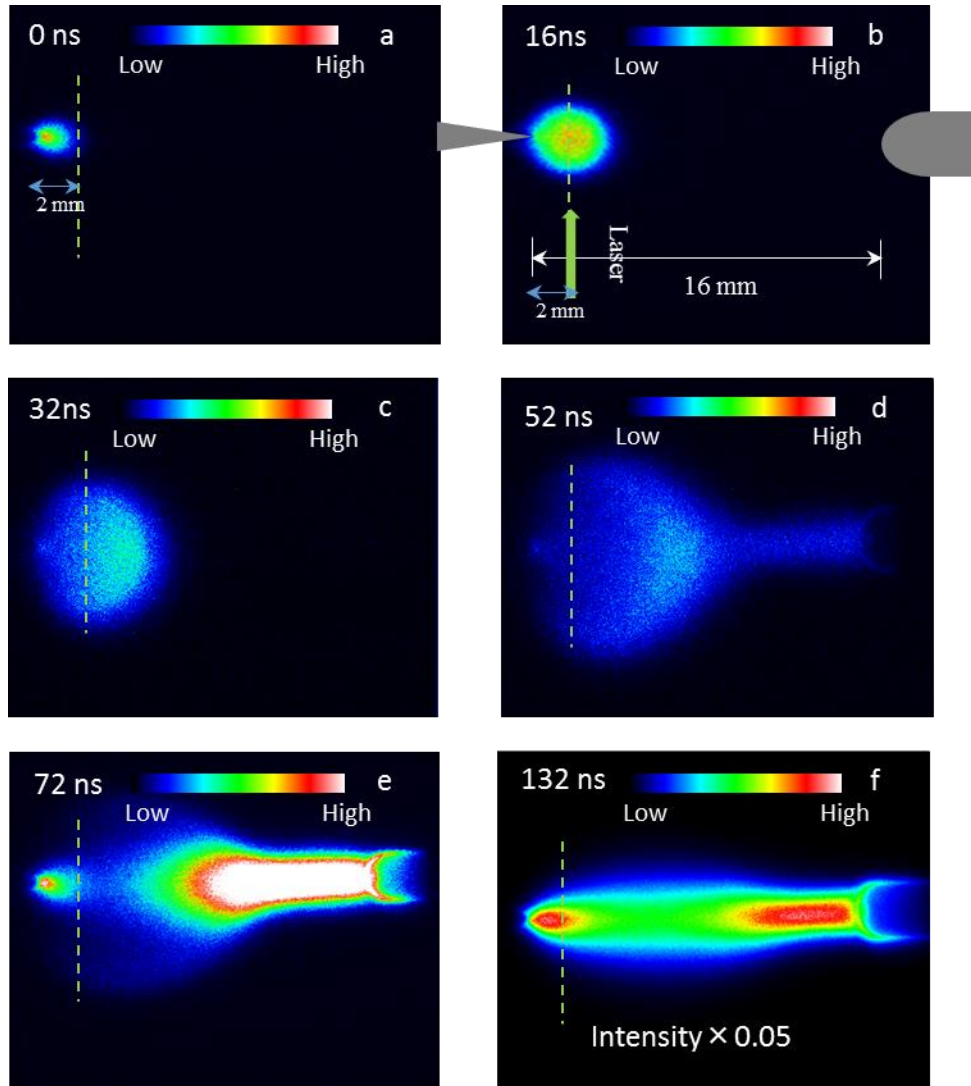

Fig.4.1. Time evolution of the cathode-directed streamer in helium gas. The images were captured by ICCD camera. The colors of images are artificial and show signal intensities. The ICCD camera covered the wavelength range from ultra-violate to near infra-red. (a) the streamer starts from the tip of the needle electrode. (b) (c) (d) (e) it expands as a shell toward the hemispherical electrode at a distance of 16 mm. (f) the secondary streamer.
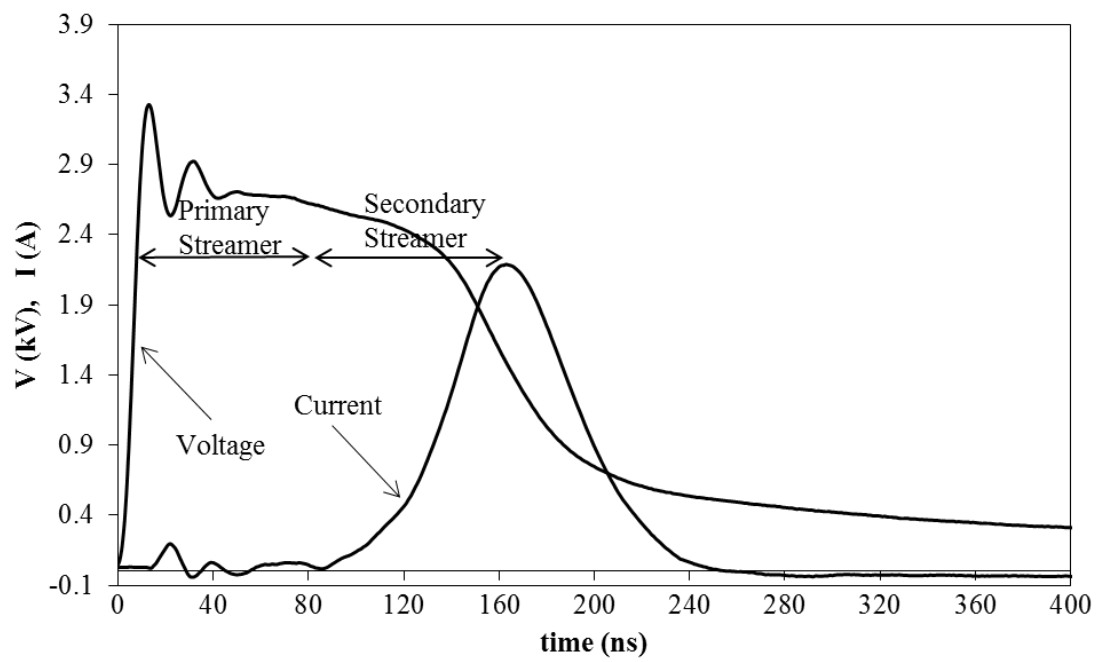
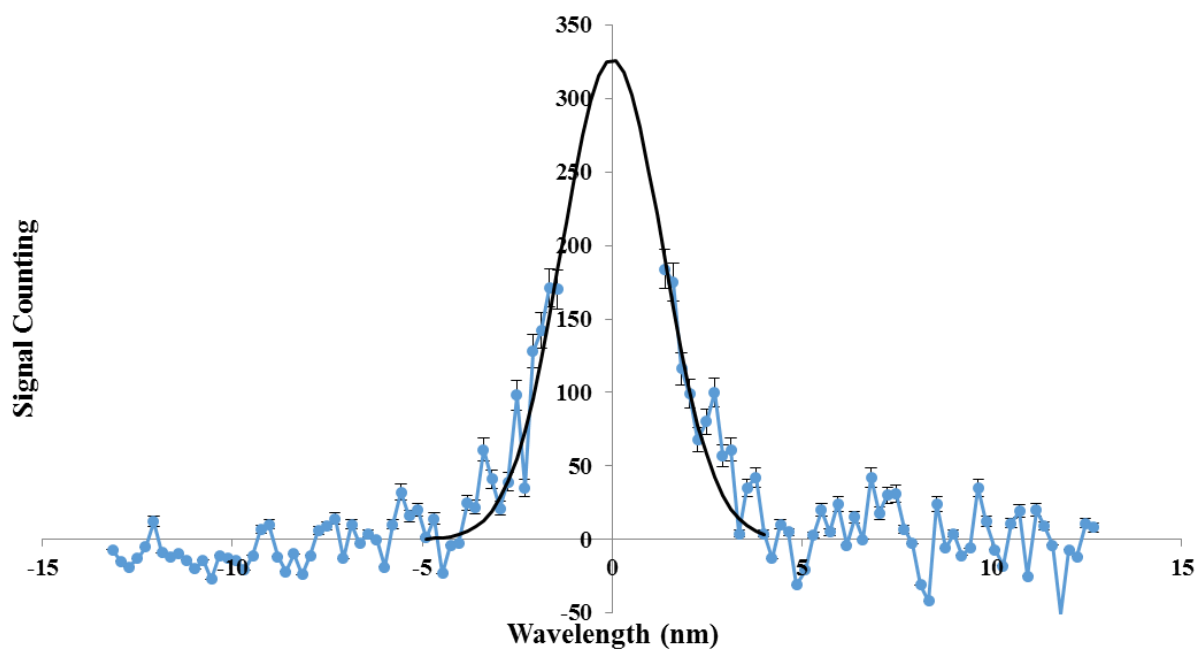Fig. 4.2. Voltage and current waveforms.

Fig.4.3 An example of measured LTS spectrum. A full line is a fitted Gaussian curve.

Yamamoto et al. [24] reported that the Thomson scattering signal is affected by the photo-ionization of metastable xenon atoms when the laser power density is greater than 10^{15} W/m^2. Chen et al. [25] also showed that the photo-ionization of metastable argon atoms affects the Thomson scattering spectrum when the power density of the probing laser is greater than 4×10^{13} W/m^2. For the case of the streamer, due to the very high electric field, the effect of the photo-ionization of all excited atoms must be taken into account. In order to examine the effect of the laser perturbation, the dependence of the signal intensity on the laser power density was investigated. In this investigation, we changed the laser beam focusing system from a usual plano-convex lens to the combination of two cylindrical lenses whose setup will be shown later. The essential point here is that the beam spot of the probing laser by the two cylindrical lenses had a diameter of 0.2 mm which is much larger than the spot diameter size of 50 μm by the initially used plano-convex lens. Using the new laser focusing system, the probing laser energy was changed in the range from 10 mJ to100 mJ. The result is shown in Fig. 4.4. This measurement was done at t = 16 ns when the laser beam hit the streamer head. The figure shows that the signal intensity is linear to up of 1.3×10^{14} W/m^2 and above that power density, the signals clearly deviate from the linearity. Therefore, Thomson scattering measurements must be performed below the laser power density of 1×10^{14} W/m^2.

Based on the above result, we decided to set the laser spot size to be 0.2 mm×1 mm (actual shape is elliptical) for the further measurements of this study. The setup of the two cylindrical lens system was taken as shown in Fig. 4.5. As shown in Fig. 4.1(b), the laser beam is injected from the bottom side of the paper to the upper side. The laser spot size of 0.2 mm is in the direction of the streamer development (left to right). The scattered light is collected using the sight line which is 90 degree perpendicular to the paper surface, and the spot size of 1mm is in this direction. In order to have a clear LTS spectrum, the laser energy increased up to 100 mJ. In this case, the laser power density is 5×10^{13} W/m^2. This value is well below the threshold for the laser perturbation. The LTS spectrum shown in Fig. 4.3 was obtained using this setup.
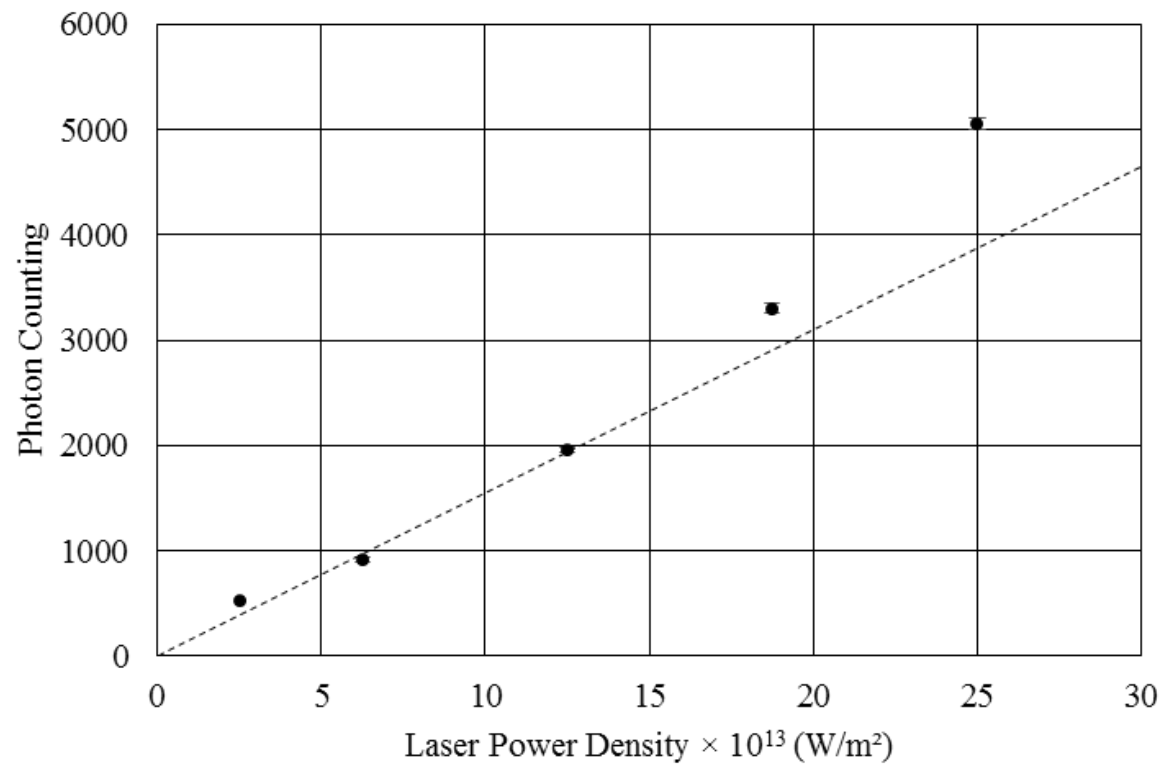
Fig. 4.4 Signal intensity of the Thomson scattering as a function of the laser power density.
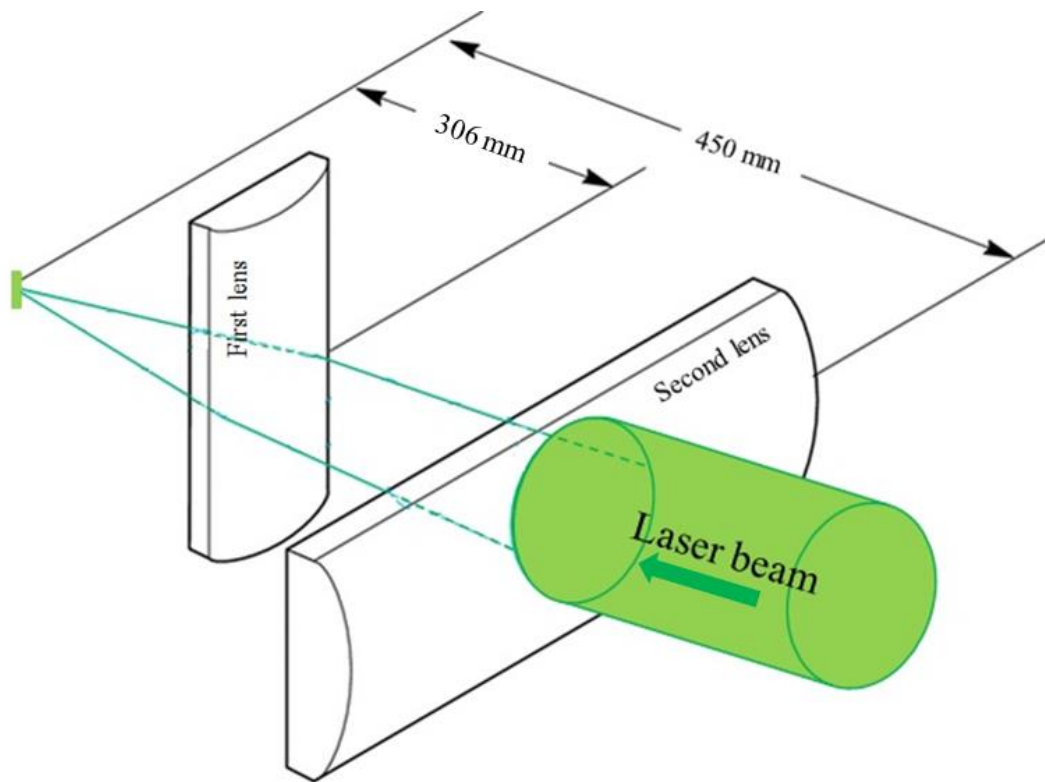
Fig. 4.5 Setup of cylindrical lenses system to shape the laser spot size (the vertical spot size of 1 mm and the horizontal spot size of 0.2 mm). The axis of the second lens (focal length of 400 mm) axis is perpendicular to that of the first lens (focal length of 300 mm).

Figure 4.6 shows temporal evolution of n_e and T_e at a point 2 mm from the needle electrode. At t=16ns, the electron temperature is around 2 eV. At this time the laser beam hit the head of the streamer as shown in Fig.4.1 (b). As time passes, T_e decreases to reach the value of 0.83 eV at t=36ns. On the other hand, n_e is about 3×10^{18} m^{-3} at this time interval, and after that, it decreases to 1×10^{18} m^{-3} at t=56ns. This behavior shows that the electron temperature and electron density have their maximum values at the head of the streamer. It is reported [2] that, in front of streamer head, the external and internal electric fields add up to make a stronger total field, which boost ionization. Thus, intense ionization and excitation of gas atoms occur in this region. This could be a strong reason why the light emitted in the streamer head appears in the ICCD images of this experiment (Fig 4.1. (b), (c), (d)). On the other hand, inside the streamer or the plasma channel behind of the streamer head, the total electric field become weaker, which may slow down the ionization [23]. These features of the streamer are consistent with our observations. Also, the measured values of n_e are rather close to simulation results of the helium streamer at the atmospheric pressure in Ref. 23 and Ref. 26. At t=72ns, the streamer channel reach the hemispherical electrode (Fig. 4.1 (e)), so the electrical current significantly increased to form a secondary streamer. From this time, T_e and n_e increase dramatically until 140ns (Fig. 4.6 (a) (b)).

4.4 Conclusion

We have developed the LTS method to diagnose the streamer. In order to avoid the laser perturbation, we optimized the laser spot size by using two cylindrical lenses. Because we could utilize a relatively large laser energy without the laser perturbation, we could clearly detect LTS signals and measure values of n_e and T_e of the streamer for the first time. Also, temporal evolution of n_e and T_e measured at a point 2 mm from the needle electrode are consistent with reported results of the streamer simulations.
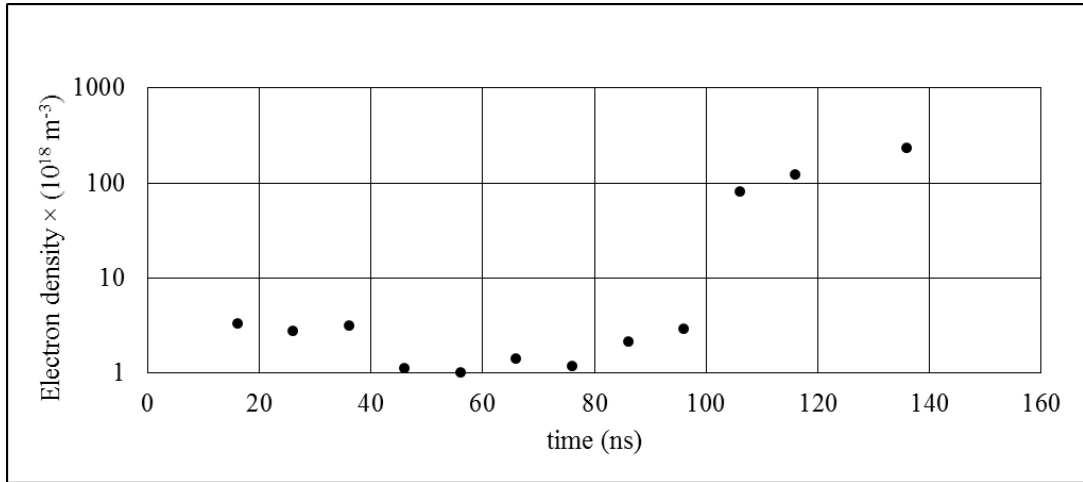
(a)
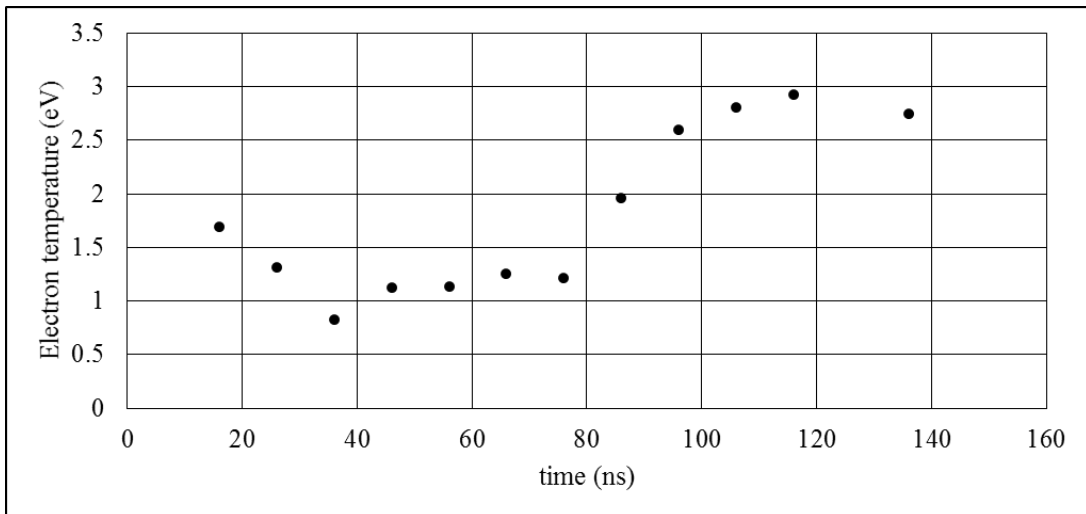
(b)

Fig. 4.6 Temporal evolution of a) electron density and b) electron temperature of the streamer.

The measured position is at 2 mm from the needle electrode.

References

[1] L. B. Loeb and J. M. Meek, the Mechanism of the Electric Spark (Oxford University Press, Oxford, 1941).

[2] M. C. Wang and E. E. Kunhardt, Streamer dynamics, Physical Review A, 42, 2366 (1990).

[3] U. Ebert, W. Saarloos, and C. Caroli, Streamer Propagation as a Pattern Formation Problem: Planar Fronts, Physical review letters, 77, 4178 (1996).

[4] V. F. Tarasenko, Generation of Ionization Waves and Streamers in Gases at Elevated Pressure, Russian Physics Journal, 51, 656 (2008).

[5] V. A. Davidenko, B.A. Dolgoshein, and S.V. Somov, Experimental investigation of streamer discharge development in neon, Soviet Physics JETP, 28, 227 (1969).

[6] T. M. P. Briels, E. M. van Veldhuizen, and U. Ebert, Experiments on propagating and branching positive streamers in air, XVth Int. Conf. on gas discharges and appl., 2004.

[7] T. M. P. Briels, E. M. van Veldhuizen, and U. Ebert, Branching of positive discharge streamers in air at varying pressures, IEEE Trans. On Plasma Science. 33, 264 (2005).

[8] T. M. P. Briels, E. M. van Veldhuizen, and U. Ebert, Time resolved measurements of streamer inception in air, IEEE Trans. On Plasma Science. 36, 908 (2008).

[9] E. M. van Veldhuizen, S. Nijdam, A. Luque, F. Brau, and U. Ebert, 3D Properties of pulsed corona steamers, The European Physical Journal Applied Physics 47, 2 (2009).

[10] Yu. V. Shcherbakov, and L. I. Nekhamkin, Accurate spectroscopic studies of streamer discharge. 2. Theoretical background and analysis, Annual Report Conference on Electrical Insulation and Dielectric Phenomena, 2005, p. 593.

[11] Y.L.M. Creyghton, Diagnostic techniques for atmosphere streamer discharges, Science, measurement and technology, IEEE Proceedings. 141, 1994, p. 141.

[12] R. Ono, and T. Oda, International Journal of Plasma Environmental Science and Technology. 1, 123 (2007).

[13] R. Ono, and T. Oda, Journal of Applied Physics. 97, 013302 (2005).

[14] S. Hassaballa, M. Yakushiji, Y. K. Kim, K. Tomita, K. Uchino, and K. Muraoka, IEEE Trans. Plasma Sci. 32, 127 (2004).

[15] K. Tomita, T. Kagawa, K. Uchino, S. Katsuki, and H. Akiyama, J. Plasma and Fusion Research 8, 488 (2009).

[16] S. Hassaballa, Y. Sonoda, K. Tomita, Y-K Kim, and K Uchino, J. Soc. Information Display 13, 639 (2005).

[17] S. Hassaballa, K. Tomita, Y. K. Kim, K. Uchino, H. Hatanaka, Y. M. Kim, C. H. Park, and K. Muraoka, Jpn. J. Appl. Phys. 44, L442 (2005).

[18] Y. Sonoda, S. Nishimoto, K. Tomita, S. Hassaballa, Y. Yamagata, and K. Uchino, J. Plasma and Fusion Research, 8, 696 (2009).

[19] K. Tomita, S. Hassaballa, and K. Uchino: IEEJ Trans. FM, 130, 1099 (2010).

[20] K. Tomita, N. Bolouki, H. Shirozono, Y. Yamagata, K. Uchino, and K. Takaki, J. Instrum. 7, C02057 (2012).

[21] A. Fridman, Plasma Chemistry (Cambridge University Press, 2008)

[22] A. Chirokov, Self-organization of micro-discharges in DBD plasma, a thesis of Drexel University. Nov. 2003.

[23] J. P. Boeuf, L. L. Yang, and L. C. Pitchford, J. Phys. D, Appl. Phys. 46, 015201 (2013).

[24] N. Yamamoto, K. Tomita, K. Sugita, T. Kurita, H. Nakashima, and K. Uchino, Review of Scientific Instruments, 83, 073106 (2012).

[25] W. Chen, K. Ogiwara, K. Koge, K. Tomita, K. Uchino, and Y. Kawai, Plasma and Fusion Research, 8, 1306114 (2013).

[26] G. V. Naidis, J. Phys. D: Appl. Phys. 43, 402001 (2010).

Chapter 5

Conclusions

The main purpose of the research described in this thesis is applying laser Thomson scattering method to measure plasma parameters such as electron density and electron temperature in dielectric barrier micro discharge and the early stage of breakdown voltage (primary streamer) with high spatial and temporal resolution.

Generally, the electron density and temperature in typical plasma play key role in ionization mechanisms, including electron impact and recombination as well as chemical reactions. Thus, the knowledge of the plasma parameters is so important to evaluate such mechanisms. One of the most reliable and precise methods of monitoring these parameters is laser Thomson scattering (LTS) diagnostics system. Since diagnostics of micro-discharges forming the DBD plasmas are very difficult, characteristics of such plasmas have not yet been understood well. DBD plasmas are initiated in large number micro-discharges filaments of nanosecond duration. Therefore, detailed measurement of one pulsed filament discharge is important for understanding of DBD. However, direct measurements of DBD parameters are very difficult, because the life time and radius of the micro-discharges are lower than 100 ns and 100 μm, respectively. Moreover, they are produced randomly both in time and position. As the first step of research, we selected capacity coupled discharge (CCD) as a non-thermal atmospheric pressure plasma instead of DBD to determine diagnostics of the pulsed filament discharge. Due to the CCD circuit does not have a dielectric layer between discharge electrodes, we could control the formation time and the spatial position of the CCD plasma. For the measurements of spatial distributions of n_e and T_e, five axial positions were selected. $z=0$ means the center of the electrode gap and $z=100$ μm and 200 μm are for the needle electrode side and $z=-100$ and -200 μm are for the hemispherical electrode side

- The LTS method was successfully applied to the CCD plasma and measurements of spatial distributions of n_e and T_e of the pulsed filament discharge were demonstrated at $t=15$ ns, 55 ns, 105 ns, and 205 ns.

- n_e is peaked near the tip of the needle electrode (z=200 μm) where the electric field concentrates, and the value exceeds 10^{23} m^{-3}. On the other hand, even at the same time the n_e near the hemispherical electrode (z= -200 μm) is 10 times lower than that at z=200 μm, and the spatial distribution is flat over 500 μm while the spatial distributions of T_e at z=100, 0, -100, and -200 μm are flat and the values are around 1.5 (±0.5) eV. At t=55 ns the power input to the CCD is truncated. The value of n_e starts to decrease and T_e decreases about 0.9 eV. Finally at t=205 ns both of n_e and T_e take the same values in all places.

- At the center of the discharge, n_e and T_e has been estimated to be 4.6 ($\pm$ 0.6)×10^{22} m^{-3} and 1.7 ($\pm$ 0.3) eV, respectively, at the time of 15 ns after the start of the discharge. It has been found that the transient behavior of the pulsed CCD is dominated by the three-body electron-ion recombination because of high electron density as well as electron-ion dissociative recombination due to the formation of dimer ion in high pressure. Both of these mechanisms are operative in this system. It has also been found that the pulsed CCD is maintained in non-thermal state for a long time more than the thermal relaxation time that elastic collision became predominant. Finally, the results show that the LTS can be the powerful method to diagnose non-thermal atmospheric pressure plasmas.

- LTS measurements have been successfully performed on the pulsed filament micro-discharge of DBD. Temporal evolution of electron density and temperature could also be measured. It has been investigated that the peak values of electron density and electron temperature at the center of the pulsed filament discharge are (1.03 ±0.08)×10^{22} m^{-3} and 2.62 (±0.2) eV, respectively. It was also found that the behavior of the micro-discharge of DBD is governed by the three-body recombination and dissociative recombination.

- For all cases (different total charges), the electron density is almost the same before 30 ns. After that, it decreases with a time constant of 100 ns. This decay time is consistent with three body recombination and dissociative recombination. Increasing of total charges leads to increasing electron density; however, electron temperature does not change significantly.

We developed LTS method to diagnose streamer plasmas. As a result, temporal evolution of electron density and electron temperature has been measured at 2mm from the needle electrode.

In order to avoid the laser perturbation, the laser spot size was optimized by using two cylindrical lenses. Since a relatively large laser energy without the laser perturbation was utilized, the LTS signals were detected clearly and the values of n_e and T_e of the streamer were obtained for the first time.

- At t=16 ns, the electron temperature is around 2 eV. As the time passes, T_e decreases to reach the value of 0.83 eV at t=36ns. On the other hand, n_e is about 3×10^{18} m^{-3} at this time interval, and after that, it decreases to 1×10^{18} m^{-3} at t = 56ns. This behavior shows that the electron temperature and electron density at the head of the streamer have the maximum of values.

- At t=70ns, the streamer channel reaches the hemispherical electrode, so the electrical current significantly increase to form a secondary streamer. At this time, T_e and n_e increase dramatically until 140 ns.

Basically, laser Thomson scattering diagnostics can be applied for all gases of plasma discharge. However, due to rotational and vibrational states in molecular gases, noble gases have simple spectrum compared to molecular gases. Therefore, as first step in micro-discharge investigation, analysis of Thomson scattering spectrum in noble gases is easier. The next step of our research is applying this technique to discharges in molecular gases such as nitrogen and oxygen.

In future investigation in streamer phase, we must consider the directional dependence of wave vector of incident probe laser beam and external electric field. These two vectors are perpendicular in current experiment that might effect in LTS measurement, because the electrons in streamer phase accelerated in electric field direction. Therefore, we are going to rotate electrode setup to change the angle of incident wave vector and electric field.